

Growth Towards Light:  
Translation of Optical Inputs into  
Mesostructured Outputs via Inorganic Phototropism

Thesis by  
Azhar Iqbal Carim

In Partial Fulfillment of the Requirements for  
the degree of  
Doctor of Philosophy

CALIFORNIA INSTITUTE OF TECHNOLOGY  
Pasadena, California

2021  
(Defended 28 January 2021)

© 2021

All Rights Reserved

Azhar Iqbal Carim  
ORCID: 0000-0003-36306872

## ACKNOWLEDGEMENTS

A close friend recently told me that the “dessert” of generating a dissertation is the opportunity to write the acknowledgments. In fact, composing the text in this section is a pleasure that I first started contemplating well before I ever submitted any application for admission to a graduate degree program. Midway through my undergraduate studies I found myself fortunate enough to have already received the opportunity to work with many individuals that contributed to my growth both inside and out of science. As I received my degree and progressed through my doctoral work, this list persistently became ever longer. Now, as I place a coda on the doctoral phase of my career and at last bring the words to a page, I am in awe of all the amazing interactions I have had, the support I have received, the friendships forged, and the countless memories made along the way.

First and foremost, I am extremely thankful for my amazing family. They have always worked to provide me all the resources to succeed and shaped me into someone capable of pursuing a doctorate at Caltech. They encouraged me as I moved several thousand miles across the country to study in Pasadena and then consistently supported me, never wavering, throughout the years of my graduate work. I am extremely happy that they can know that I have earned a doctorate.

I am grateful for having high school science teachers that helped me build the knowledge and spark the curiosity that served as the foundation for all my subsequent studies. Kevin Meisner (AP Chemistry) and Steve Dail (AP Physics) were excellent instructors with a genuine passion for education.

As an undergraduate at the University of Michigan, I was lucky to join Stephen Maldonado as the first student in his new lab. I remember having our initial conversation in his

office as he first installed Windows on his office computer. He taught me electrochemistry and all the ins and outs of the lab himself. Then, as the group took shape, I was afforded a unique freedom to work independently and lead my investigations. As my projects advanced Stephen mentored me on how to make figures, write scientific papers, and navigate the publication process. When I was choosing potential graduate programs Stephen suggested I add Caltech to the list. Stephen has an amazing ability to conceive a potential storyline and associated manuscript before any results are collected, enabling targeted research and motivating students to pursue the project with clear goals. Thus, a great amount of the success I had during my doctoral work can in part be attributed to the mentorship I received from Stephen.

The early edition of the Maldonado group was a close-knit, collaborative and supportive community, a group of friends who were also intense researchers: an amazing place to cut my teeth as a scientist. Michelle Chitambar was the first official graduate student and offered a model of effectiveness. Jhindan Mukherjee, our sole postdoc for a while, was always a friendly presence and free to talk about anything. Kevin Hagedorn joined the lab as a senior student and taught me several tips and tricks. I worked closely with the industrious Junsu Gu who helped greatly in carrying out *in situ* SERS work. Sean Collins was an extraordinary undergraduate and skilled electron microscopist, and was an indispensable collaborator in the discovery and analysis of ec-LLS growth. I met Jeremy Feldblyum when he was a young graduate student but he clearly already had the heart of a professor and provided me with all sorts of scientific and academic tidbits. Sabrina Peczonczyk helped keep me in line and her presence always helped make being in lab a good time. I look back fondly on many nights on South U with Sean, Jeremy and Sabrina. Wen Wen often provided a unique brand of humor. Justin Foley helped perform device measurements for the initial ec-LLS work and was a reliable source of levity and laughter in the lab. Eli Fahrenkrug joined the group soon after I left but was a great companion at many

conferences as we both studied electrodeposition as graduate students, and I had the opportunity to watch as he continued with the ec-LLS research, expanding the scope and taking the science to exciting new heights.

Bart Bartlett's group was established at Michigan at the same time as the Maldonado group and took the role of our "sister" group, in many ways an extension of our own. Together we shared equipment and supplies, discussed science, collaborated and celebrated. Tanya Breault, Xiaoguang Hao and Joe Yourey were early members of Bartlett group that I had the pleasure of getting to know and helped me in various ways.

My undergraduate projects often found me in the lab of Adam Matzger. Matzger would often make rounds, strike up a conversation, and provide advice and experimental help as if I was his own student. I am thankful for the assistance of Vilmalí López-Mejías and Kira Landenberger on the Raman systems and of Antek Wong-Foy on the XRD instruments.

Al Wilson, George Johnston and Steve Donajkowski in the Michigan Chemistry instrument shop all provided excellent expertise and helped me succeed in my research efforts despite my then limited skills as a maker.

I was extremely lucky to have the support of Roy Wentz, glassblower extraordinaire who showed amazing dedication and generosity. I warmly remember sitting down with Roy at his desk to for a "R&D" session in which I would bring him my experiment and he would devise a solution, but only after first offering me a cold drink. Then, I'd often be reminded to come back just before four o'clock when I would find whatever we had just designed already full realized and almost ready to come out of the annealing oven.

Beverly Lange wore many hats as Michigan Chemistry's undergraduate coordinator and I am thankful for the cheer and support she provided in all of these roles.

When I first arrived on campus in Pasadena, I often heard the phrase “Caltech is a special place” yet did not understand what it meant: it seemed not much more than trite and cliché expression. However, as I complete my doctoral work, I have come to learn that this saying is understood to have a precise meaning: that Caltech is a place where dynamic, talented people are brought together and provided an amazingly open environment and immense and incomparable latitude to pursue their curiosities in whatever manner they see fit, resulting in the spontaneous production of fantastic innovation and scientific excellence. I am extremely appreciative of my adviser, Nate Lewis, who has always strived to maintain this ideal with marked dedication and persistence. He provided me with great freedom from the start and at the same time was ready and able to offer support whenever needed, and always supplied encouragement. Nate charts his own path towards his goals and encourages everyone he works with to do the same.

I am very thankful that Barbara Miralles joined the group before me as she has served as a constant presence throughout my tenure always being unbelievably great at doing everything the group needs to run. Barbara has been a consistent source of support and it is always good to know that she is just a phone call away. I look forward to dropping by her office to hang out and chat many more times in the future.

I was fortunate to have an excellent team serve on my doctoral committee. Geoff Blake acted as the committee chair and provided insightful critiques of my proposals. Prior to joining my committee, George Rossman welcomed me into his lab and openly provided me access to his Raman microscope and other analytical tools. He was always happy to provide instrument assistance, discuss science, and let me borrow optics whenever I needed them. As a member of my committee, I have greatly valued his genuine scientific interest and curiosity. Harry Gray has always been more than willing to provide support whenever I need it and I am deeply grateful

for his consistent eagerness to talk and always open office door as well as the energy and enthusiasm he brings to every meeting.

I am extremely thankful for the support afforded to me by Harry Atwater and his group. Much of my doctoral research, including all the science presented in this thesis, has been enabled by collaboration with the Atwater group.

When I first came to the Lewis group, I remember talking with different members to explore the science that was underway and when I met with Bryce Sadtler about the phototropic project I immediately knew what I wanted to work on. I am indebted to Bryce for providing me with an amazing foundation to work from and getting me started in the lab and on a path to success. He also opened his bench space to me, let me use all his experimental apparatus, helped me gather supplies, and introduced me to the self-organized structures subgroup, the LMI-EFRC and the Atwater group.

I was lucky to join the Lewis group as part of a large cohort and am glad today that Noah Plymale, Nick Batara, Michael Lichterman and myself are all doctors and friends.

Nick was my key partner for many years and a great friend. Together we spent countless hours in discussion as we strove to decipher the mysteries of phototropic growth. Nick helped me learn a great deal about photonics and electromagnetism. Only through the combination of his modeling and theory work with my experiments were all the advances and conclusions presented in this thesis made possible. Fortunately, each of us believed that the other had the more challenging part of the project.

Lichterman and I collaborated on wide array of projects over the many years we shared. I was impressed by Lichterman's ability to effortlessly move between initial investigations at amazing speed to rapidly ascertain the potential success and novelty of a project. I appreciated his dedication to the mantra of "work hard, play hard" as well his eagerness to take full advantage

of the excellent opportunities and flexibility afforded to us as graduate students. I remember late nights of synthesizing nanoparticles interleaved with trips to Mexican restaurants. Together we also traveled across the country presenting at scientific conferences while also making sure to explore the host city. Emblematic of Lichterman's straightforward and honest style, he coined the now common nickname for phototropic growth, "squiggles".

Fadl and I worked together to complete several projects investigating electrocatalysts for sustainable hydrogen production. At the start of my doctoral studies I had not considered doing such research but got interested and picked it up in large part by spending time working at the bench next to Fadl's. Fadl had an impressive ability to assess risk-reward tradeoffs that he leveraged to maximize productivity which now I see is clearly a part of my own scientific approach. I am thankful for Fadl's outgoing nature and broad network, as a result he kept me connected in and out of work and introduced me to a great number of ideas, people and places, and continues to do so today.

Jonathan and I were collaborators on series of squiggles investigations. Jonathan was extremely smart with a broad knowledge base, the very type of person someone first imagines when thinking of the name "Caltech". He was likely almost always the smartest person in the room yet was also always down to Earth and demonstrated intense humility. Jonathan was usually my go to person if there was something that I couldn't understand or explain or something that I needed to do but didn't know how. Fortunately for me Jonathan was extremely kind and generous and helped me out time and time again.

Though Jonathan arrived at Caltech and joined the group two years after Lichterman, Fadl and I, it has hard to remember a time when he did not feel like part of our class. Together we all explored Los Angeles, learned to precision cook steaks sous vide, kept up with college football, and potentially exceeded the maximum payload capacity of my car several times. At a

point, it felt the TV show *Friends*, where people would drop by unannounced and open the door to my apartment assuming they'd find the others hanging out. I feel extremely lucky to have found such a set of close, lifelong friends.

Jesús Velázquez passion and motivation were a pleasure to have in the lab. Jesús took me on my first tour of Jorgensen and helped me start using the facilities there and connect with the JCAP team. Jesús was always excited to discuss new science and consistently provided encouragement and optimism.

Stefan Omelchenko was an excellent office mate and consistently provided a lively presence and good conversation.

Manny Soriaga gave me a second home in the HetCat-S group in JCAP (the Soriaga group at Caltech). Manny was an exacting scientist and at the same time full of color and constant source of humor. He was a fan of outings and celebrations: I fondly remember First Friday lunches and spreads from Porto's. Manny had assembled a tight-knit group of bona fide electrochemists and surface scientists. Jack Baricuatro knows all the old school electrochemistry tips and tricks and always shows great kindness and willingness to offer assistance. Kyle Cummins was an excellent maker and was always ready to grab tools and help build or repair.

Dan Torelli and I both spent time in Manny's HetCat group and I appreciated his carefree and fun-loving demeanor both inside and out of work. We had many good times often alongside Fadl and Lichterman.

I was lucky to have had the opportunity to mentor Anjali Premkumar. We started working together at the end of her freshman year at Caltech and her talent was immediately obvious. She quickly pioneered the investigations of phototropic growth using plural optical inputs and her experimental work contributed largely to the data presented in this thesis. Anjali also brought uplifting cheer and enthusiasm into the lab each day.

Annelise Thompson and I worked together on several graphene projects. I admired her tremendous work ethic and constant commitment to achieving success. She had a great sense for planning science and then methodically executing to meet objectives. Today, I miss hanging out with Annelise and Jonathan late into the night, talking and devouring bowls of popcorn.

Ethan Simonoff started by working on the “trees” project and then branched out to eventually discover new insights into inorganic phototropic growth that informed our later work. He was also key in bringing initial modeling workstation online and functional. Ethan was a wonderful source of irreverence and boisterousness. Together with Jonathan, we had a great time exploring all the coffee shops in and around Pasadena.

I happy to have mentored and worked with Kat Rinaldi pioneering new *in situ* Raman investigations of surface science and electrocatalysis, as well as *in vivo* analysis of live cells. I'll always remember the day we realized that cells can move. Kat always displays a down to earth personality and relaxed nature that I always appreciated yet also has an awesome vivaciousness with the ability to stir up conversation in any room. She can also “bully” me and keep me check.

Mita Dasog and I worked together to image via electrodeposition the spatial profile of photocarriers in semiconductor microwires and quickly grew close. Mita was exceptionally talented, and when I met her, already very extremely accomplished, yet always maintained a great sense of humility. Mita was extremely industrious, and I enjoyed the company of another night owl. She persistently exhibited great kindness and was always open to invest time and energy to collaborate, work hands-on, and help others scientifically even if a return was not expected. Mita has provided me a great deal of support and served as a role model both academically and generally.

Sisir Yalamanchili worked with Mita and I on the microwire electrodeposition project and together as “Team B” we had a lot of fun as we moved the project along. Later, Sisir helped me often when I had questions on photonics, electromagnetism and associated computer modeling, and helped frequently with taking care of clean rooms tasks. He also believed in the “work hard, play hard” lifestyle and was always open to trying new things. Together, we worked many odd hours and found ourselves on many adventures as we became close friends. Sisir was also a consistent source of humor, delivering many quotable lines that will never be forgotten.

I worked with Paul Kempler at the beginning of his graduate career along with Mita and Sisir as he started to get his microwire projects off the ground. Paul was smart and productive as well as passionate and fun-loving: always great to have around.

Mentoring and collaborating with Katie Hamann has been a great pleasure. I have tremendous respect for Katie’s hardworking ethos, perseverance, and commitment to reaching excellence. I also admire that at the same time she manages to be compassionate, generous, and warmhearted. Katie has been a phenomenal partner, an ideal counterpart, and has always driven me to achieve and improve. I also appreciate that she is always there to provide support. I remember sitting with Katie outside of Red Door Café at the start of her first year, encouraging her to take a leap of faith and work on phototropic growth with me. She jumped in with both feet and immediately started making major advances with squiggles and never stopped, and along the way I gained a great friend. I more than enjoyed every part of this journey from seeing her set the record candidacy time, to remaining steadfast together through long nights of squiz, through AFM days with typing tests and sticky note alignments, and to many nights playing with the torch.

I first met Madeline Meier when I took her out to lunch alongside Jonathan and Katie on the first day of her summer rotation with the group prior to her first year. There, I remember

we first introduced her to squiggles as Jonathan told her to “picture a sea anemone”. She did not start on squigz just then but after that lunch we did quickly become great friends, and so when several months later when she told me she intended to join the group and was enthusiastic about squigz, I was thrilled. Today, I am extremely thankful that I have been able to mentor Madeline. She is talented, resourceful, and always jovial. Only a few weeks into her first project we bet on a conference abstract, submitting our hypothesized results and analysis, and several months later I got to see her present a complete story at a national meeting before even giving her first group meeting. Moreover, I am very appreciative that Madeline signed on to so many adventures and antics including driving all around LA to get the right picture of a tilted palm tree, learning to make burnt tortilla syrup and designing UFO themed artwork for scientific publications. She also stuck with me in solidarity on the correct side of BI 115. Additionally, Madeline has always been willing to help with whatever task I suddenly find myself needing to complete, often with short deadlines.

I am also very grateful for the chance to come together with Katie and Madeline to form squigz team. It is an amazing experience to work as a single cohesive unit wherein the whole is truly greater than the sum of the parts and the magnitude of what can be accomplished is exponentially greater than what any individual can. Simultaneously, there is comfort in knowing that any task or challenge can be borne by the team and that each person is never alone. Additionally, being close friends outside of work meant that all time at task was enjoyable and often relaxed. Sisir Yalamanchili was also often an honorary member, with contributions both scientifically and socially. Together, we made the rounds of coffee shops and dumpling restaurants, viewed eclipses and meteor showers, and also completed the “hat” bet, amongst much else.

Sophia Cheng was an excellent collaborator. She was a great help taking care of many of our team's nanofabrication and clean room needs, performing ellipsometry analysis, and assisting with computer simulations of optical processes. I admired her relentless work ethic and enjoyed her company on many late nights.

I am grateful that Matthias Richter decided to join Caltech full time after initially working at JCAP as a visitor. He presents a combination of great smarts and knowledge, extensive experience, and helpful disposition that make him an invaluable resource. He has been exceptionally helpful in the setup and management of the computer systems for our modeling work as well as generating all the MATLAB code needed for data analysis. Recently, Matthias has often been the person I go to for whatever I need scientific help and am not sure of the solution.

Michael Mazza (S.S. Slammer, D.D. Detective, Zoom-Zoom) quickly fit in as a Noyes boy and has managed to keep that spirit alive with his unique jocular and whimsy. I am grateful for all he has done to make fun happen outside the lab.

Sean Byrne is currently the newest person investigating phototropic growth. Sean is dependable and diligent and also jovial and I am excited to see him make new advances.

Kimberly Papadantonakis served simultaneously in many different roles in the group. Her position as staff in tandem with her history as a group alum often provided useful perspective in navigating the challenges of the day. Kimberly helped me with a wide range of tasks spanning from event planning to grant writing. She was always been supportive of me and consistently demonstrated strong personal desire and commitment to aiding both the professional success and personal well-being of every member of the group. I also always delighted that Kimberly shared the belief that achievements are meant to be celebrated.

I am thankful for the chance to interact with a series of excellent postdocs that provided support and acted as models of success: Shane Ardo, Rob Coridan, Shu Hu, Teddy Huang, Ke Sun, Sonja Francis, Matt McDowell and Betar Gallant. Many other fellow graduate students also contributed to making my graduate experience rich, memorable and rewarding: Emily Warren, James McKone, Joseph Beardslee, Matt Shaner, Adam Nielander, Jacob Good, Heather Audesirk, Victoria Dix, Erik Verlage, Katie Chen, Brian Chmielowiec, Paul Nunez, Chance Crompton, Josh Wiensch, Ellen Yan, Weilai Yu, Kathleen Kennedy, Mo Morla, Zach Ifkovits, Jackie Dowling and Jake Evans. Undergraduate Jackie Maslyn also deserves special mention. Additionally, I am appreciative of all the contributions Bruce Brunschwig has made supporting the group.

Throughout my doctoral studies, I held several desks amongst the different group's on campus offices and enjoyed spending time in each with their own communities and atmospheres. My base was a large time in G135 Jorgensen where I enjoyed many spontaneous large group conversations as well as one member missing photo shoots. I also had the pleasure of working upstairs alongside Madeline Meier, Sophia Cheng and Matthias Richter, an arrangement that proved extremely beneficial for the advancement of squigz work. Additionally, I always enjoyed trekking over to Noyes 220 to relax at desk, hangout and chat.

I am very appreciative of all the help I got from Ryan Jones in designing (and then frequently redesigning), 3D printing, and machining a great number of cells for photoelectrochemistry and spectroelectrochemistry.

I must thank Rick Gerhart in the Caltech glass shop for his many years of help building photoelectrochemical cells. It was always a pleasure to head down to the shop and chat.

More recently, Nate Hart has joined the shop as an excellent addition and has been a great help as well. Additionally, Mike Roy in the instrument shop is always a pleasure to work

with and helped design and along with Steve Olson helped make a series of pieces to complement our electrochemical cells.

I was lucky to be a part of the DOE-funded “Light-Material Interactions in Energy Conversion Energy” Energy Frontier Research Center (LMI-EFRC) for a large part of my doctoral tenure. It was a great opportunity to be connected with a team of very smart people doing exciting science and attending the biannual meetings and weekly seminars was always fun. I am appreciative of all the work done by Carrie Hofmann, Jennifer Blankenship, Tiffany Kimoto and Lyann Lau managing this program and must especially thank Lyann for entertaining all my pizza requests in the final years of the center.

My time as a graduate student was heavily influenced by presence of the Joint Center for Artificial Photosynthesis (JCAP), a DOE Energy Hub. I spent a significant amount of time collaborating on JCAP projects and working in JCAP facilities. I am thankful for all the opportunities and resources JCAP provided as well as all the people that JCAP connected me with. I especially enjoyed spending Friday evenings with Carl Koval, Achim Lewerenz, John Gregoire, Michael Lichterman, Kyle Cummins, Chris Karp, Ryan Jones and many others. I would like to thank Mabby Howard for all her efforts managing daily operations at JCAP.

I humbled by the magnitude of people that enabled my journey. Thank you all!

*Azhar I. Carim*  
2021  
Pasadena, CA

## ABSTRACT

Palm trees exhibit phototropic growth wherein physical extension of the plant guides the crown towards the time-averaged position of the sun to maximize solar harvesting. In analogous fashion, the directed growth and resultant nanoscale morphology of an evolving inorganic semiconductor deposit can be precisely defined in three-dimensional space using incoherent, uncorrelated light with spatially-invariant intensity. Maskless, photo-driven electrochemical deposition of semiconductor films generates highly ordered, periodic mesostructures with anisotropic, nanoscale features conformally over macroscale areas. This inorganic phototropic growth process does not utilize any physical nor chemical templating agents. Rather, as with natural phototropism, wherein the morphological phenotype expressed by an organism is a function of the light available in the habitat during growth, the precise mesostructures are set by the deposition illumination. Structural complexity and anisotropy result as consequences of inherent asymmetry in the light-material interactions during growth. Here, the morphological outcomes defined by specific illumination inputs are explored and the microscopic optical phenomena underpinning this physical recording of light information is interrogated via both experimental and computational methodologies.

## PUBLISHED CONTENT AND CONTRIBUTIONS

**Self-Optimizing Photoelectrochemical Growth of Nanopatterned Se-Te Films in Response to the Spectral Distribution of Incident Illumination**

Carim, A. I.; Batara, N. A.; Premkumar, A.; Atwater, H. A.; Lewis, N. S. *Nano Letters*, **2015**, *15*, 7071-7076. DOI: 10.1021/acs.nanolett.5b03137

A.I.C. designed the study, conducted experiments, and wrote the manuscript.

**Polarization Control of Morphological Pattern Orientation During Light-Mediated Synthesis of Nanostructured Se-Te Films**

Carim, A. I.; Batara, N. A.; Premkumar, A.; Atwater, H. A.; Lewis, N. S. *ACS Nano*, **2016**, *10*, 102-111. DOI: 10.1021/acsnano.5b05119

A.I.C. designed the study, conducted experiments, and wrote the manuscript.

**Morphological Expression of the Coherence and Relative Phase of Optical Inputs to the Photoelectrodeposition of Nanopatterned Se-Te Films**

Carim, A. I.; Batara, N. A.; Premkumar, A.; May, R.; Atwater, H. A.; Lewis, N. S. *Nano Letters*, **2016**, *16*, 2963-2968. DOI: 10.1021/acs.nanolett.5b04999

A.I.C. designed the study, conducted experiments, and wrote the manuscript.

## TABLE OF CONTENTS

Acknowledgements .....	iii
Abstract .....	xvi
Published Content and Contributions.....	xvii
Table of Contents.....	xviii
List of Figures .....	xix
Chapter 1: Introduction.....	1
1.1 Background.....	1
1.2 Inorganic Phototropic Growth .....	5
1.3 Overview .....	11
Chapter 2: Methods.....	12
2.1 Materials and Chemicals .....	12
2.2 Electrode Preparation .....	13
2.3 Electrode Illumination .....	14
2.4 Photoelectrochemical Deposition .....	17
2.5 Scanning-Electron Microscopy .....	18
2.6 Iterative Growth Modeling.....	19
2.7 Simulation of Field Amplitude Resulting from Dipole Emitters .....	21
2.8 Simulation of Absorption in Idealized Structures .....	22
Chapter 3: Self-Optimizing Photoelectrochemical Growth of Nanopatterned Se-Te Films In Response to the Spectral Distribution of Incident Illumination.....	23
3.1 Introduction.....	23
3.2 Results and Discussion .....	24
3.3 Conclusions.....	42
Chapter 4: Polarization Control of Morphological Pattern Orientation During Light-Mediated Synthesis of Nanostructured Se-Te Films .....	43
3.1 Introduction.....	43
3.2 Results and Discussion .....	44
3.3 Conclusions.....	66
Chapter 5: Morphological Expression of the Coherence and Relative Phase of Optical Inputs to the Photoelectrodeposition of Nanopatterned Se-Te Films .....	68
3.1 Introduction.....	68
3.2 Results and Discussion .....	69
3.3 Conclusions.....	84
Bibliography.....	87

## LIST OF FIGURES

<i>Number</i>	<i>Page</i>
1.1 Phototropic growth of palm trees.....	3
1.2 Directional inorganic phototropic growth .....	5
1.3 Simulated light absorption profiles in a model photoelectrodeposit morphology .....	6
1.4 Chronoamperometry data for light-mediated cathodic Se-Te electrodeposition .....	7
1.5 Inorganic phototropic growth with an unpatterned substrate and unstructured illumination.....	8
1.6 Schematic summarizing the optically-based iterative growth model used to computationally assess inorganic phototropic growth.....	9
1.7 Simulated morphologies for inorganic phototropic growth with an unpatterned substrate and unstructured illumination.....	9
3.1 Effect of the spectral bandwidth of vertically polarized illumination sources on the morphology of photoelectrodeposited Se-Te films .....	24
3.2 Fourier analysis of film morphologies generated with narrowband and broadband spectral distributions yielding a similar intensity- averaged wavelength.....	26
3.3 Effect of simultaneous illumination with two discrete narrowband sources on the morphology of the photoelectrodeposited Se-Te films. ....	28
3.4 Fourier analysis of film morphologies generated with single and multimodal spectral distributions .....	30
3.5 Photoelectrodeposit lamellar period as a function of the fraction of the total, two-source intensity provided by a 630 nm source utilized during growth.....	32

3.6	Computational growth modeling data representative of photoelectrodeposited Se-Te film morphologies generated using simultaneous illumination with two discrete narrowband sources .....	34
3.7	Computational analysis of light absorption anisotropy in idealized lamellar structures under simultaneous illumination with two discrete narrowband sources .....	37
4.1	Effect of illumination source polarization on orientation of photoelectrodeposit morphology .....	42
4.2	Orientation of photoelectrodeposit morphologies generated using two same-wavelength sources with differing linear polarizations .....	43
4.3	Photoelectrodeposit morphologies generated using orthogonally polarized same-wavelength sources .....	45
4.4	Photoelectrodeposit morphologies generated using orthogonally polarized sources with differing wavelengths .....	46
4.5	Normalized time-average of electric field magnitude from two dipoles emitting radiation with the same wavelength as a function of separation geometry .....	48
4.6	Normalized time-average of electric field magnitude resulting from two incoherently summed sets of dipole pairs aligned perpendicular to a direction of oscillation .....	49
4.7	Orientation of photoelectrodeposit morphologies generated using two-same wavelength sources with differing linear polarization derived computationally from growth modeling compared to experimental results .....	51
4.8	Simulated photoelectrodeposit morphologies generated using orthogonally polarized same-wavelength sources .....	53
4.9	Computational analysis of light absorption in idealized models of structures generated via photoelectrodeposition using orthogonally polarized same-wavelength sources .....	54

4.10 Computational analysis of light absorption in idealized models of structures generated via photoelectrodeposition using orthogonally polarized sources with differing wavelengths .....	56
5.1 Effect of illumination source polarization on anisotropy and orientation of photoelectrodeposit morphology .....	65
5.2 Two-source illumination polarization effect on photoelectrodeposit morphology for near-orthogonal and orthogonal polarizations .....	67
5.3 Simulated of photoelectrodeposit morphologies generated using two fully in-phase or fully out-of-phase coherent, same-wavelength sources with equal intensities and near-orthogonal or orthogonal polarizations .....	70
5.4 Effect of elliptical illumination polarization on photoelectrodeposit morphology .....	74
5.5 Orientation of photoelectrodeposit morphologies generated using elliptically polarized illumination derived from experimental results and computationally via growth modeling .....	77
5.6 Flowchart detailing expected photoelectrodeposit morphology as a function of the polarization characteristics of the optical inputs .....	79

*Chapter 1*

## INTRODUCTION

**1.1 Background**

Photochemical transformations present utility in synthetic chemistry as such mechanisms are highly specific and thus can provide control over the generated products.<sup>1</sup> Photons are extremely versatile synthetic reagents. Defining the photon wavelength determines what reactions will be promoted and defining the intensity determines the rate, and over time, the extent, of those reactions. Spatial confinement of photo-driven chemical reactions using structured illumination is the basis for several mesoscale pattern design and structure growth techniques. Photolithography, a technique used extensively to generate patterned materials and specifically in the semiconductor industry and in the production of integrated circuits, typically utilizes an optical mask to effect an illumination field with spatially-varying intensity to selectively polymerize or decompose a layer of organic photoresist applied to heterogenous substrate defined patterns.<sup>2-5</sup> A secondary step, e.g. via physical vapor deposition or dry etching, is then typically utilized to realize the pattern defined by the mask in the target material. Direct-write techniques can combine patterning and material addition or subtraction into a single processing step.<sup>6-9</sup> Such direct-writing may be accomplished by utilizing scanning laser illumination to locally drive decomposition of precursor gas promoting deposition or effect material ablation. In the same manner, pattern generation may be achieved via light-directed electrochemical processing of semiconductor substrates. The absorption of supra-bandgap photons in photoactive semiconductor substrates immersed in a metal-ion solution can provide the driving force for deposition of

the metal. This effect has been used to generate arbitrarily patterned deposits on the surface by utilization of a photomask or scanning laser illumination.<sup>10-14</sup> In such processes, localized illumination results in the spatially confined generation of mobile charge carriers which are transported toward the solid/solution interface and drive localized electrochemical deposition.

In general, photomask methods, as well as direct-write methods based on scanning laser illumination, rely on localizing light incidence and thus material addition/subtraction by manipulating the incidence of the light rather than capitalizing on inherent light-interaction anisotropies in the evolving structures during growth.<sup>6-9</sup> Approaches based on the latter phenomenon may better realize the potential power of photo-mediated synthesis by capitalizing on additional characteristics of the input light field beyond the spatial intensity profile, e.g. the wavelength, polarization, and phase. Such methods may simultaneously provide for superior accommodation of the generation of subwavelength scale features, exceeding the conventional diffraction limit, and relax the requirement for spatially structured illumination.<sup>15,16</sup> Linearly polarized light can effect photopolymerization and/or photoalignment in liquid crystal systems, generating highly anisotropic structures oriented along or perpendicular to the electric field vector.<sup>17-20</sup> Photoelectrochemical metal deposition on Si micro- and nanowire arrays can effect a wavelength-dependent spatial decoration profile.<sup>21,22</sup> The photoinduced mass transport of photoisomerizable polymers in the immediate vicinity of Au or Ag nanoparticles can generate patterns in the subwavelength regime with anisotropy dictated by the light polarization.<sup>23-26</sup> A well-studied example of light-mediated synthesis that capitalizes on asymmetrical light-matter interactions is the plasmon-mediated generation of Ag nanoparticles wherein illumination in the presence of Ag seeds and a reducing agent promotes growth of structures with surface plasmon resonance wavelengths similar to the illumination wavelength.<sup>27,28</sup> This method can generate

prisms, plates, rods, and cubes as well as other structures with high monodispersity, and provide size tuneability via control of the illumination wavelength.<sup>15</sup> Plasmon-mediated growth of surface-affixed, triangular Ag nanoparticles during illumination with linearly polarized light results in spontaneous anisotropic orientation as well as a consistent size.<sup>29</sup> This synthetic process is governed by the anisotropies in the light-material interactions resulting from sensitivity to both the wavelength and polarization of the illumination, and thus provides for the maskless generation of uniform, oriented nanostructures.<sup>15</sup>

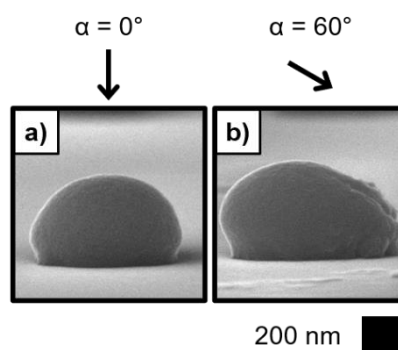


**Figure 1.1.** Phototropic growth of palm trees. In the northern hemisphere, growth towards the time-averaged solar azimuth results in a southern tilt.

Sunflowers display diurnal motion wherein leaf orientation follows the solar azimuth to optimize insolation interception.<sup>30</sup> Such motion in response to illumination is known as heliotropism and is exhibited by many photosynthetic plants, including cotton and bean, and also in the movement of several other organisms including flies and small crustaceans.<sup>31-35</sup> Significant effort has been directed towards the generation of biomimetic photoactuators that exhibit heliotropic response for a variety of purposes, including solar tracking for energy applications, remote triggering of chemical reactions, and construction of soft robots.<sup>36-39</sup>

Photoresponsive behavior is also demonstrated by palm trees which exhibit growth towards the time-averaged position of the sun to maximize solar-harvesting, resulting in a southern tilt in the northern hemisphere as the tree morphology responds adaptively to the incident illumination; Figure 1.1 presents an image of this growth behavior for palm trees in Pasadena, California.<sup>40</sup> Growth involving physical extension and material addition in a directional fashion in response to illumination is termed phototropism, and this phenomenon guides the growth of many photosynthetic species as well as other organisms such as coral.<sup>41-43</sup> The morphological phenotypes displayed by such organisms thus reflect the light available in the habitat during growth.<sup>44,45</sup> Herein, a biomimetic process based on responsive phototropic growth of materials termed “inorganic phototropic growth” is explored. Inorganic phototropic growth enables directed morphology generation via anisotropic material addition towards optical field intensity with mesostructural intricacy resulting as a consequence of the asymmetries of the light-material interactions intrinsic to the process.

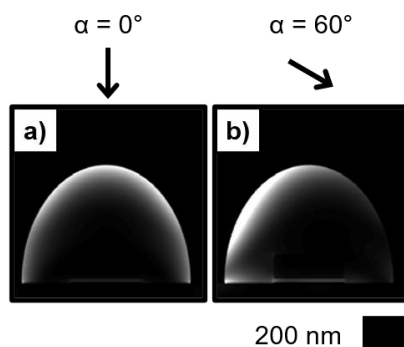
## 1.2 Inorganic Phototropic Growth



**Figure 1.2.** Directional inorganic phototropic growth. Cross-sectional SEMs representative of photoelectrodeposits generated with  $\lambda_{\text{avg}} = 528$  nm illumination incident at the indicated angle  $\alpha$  from the substrate normal.

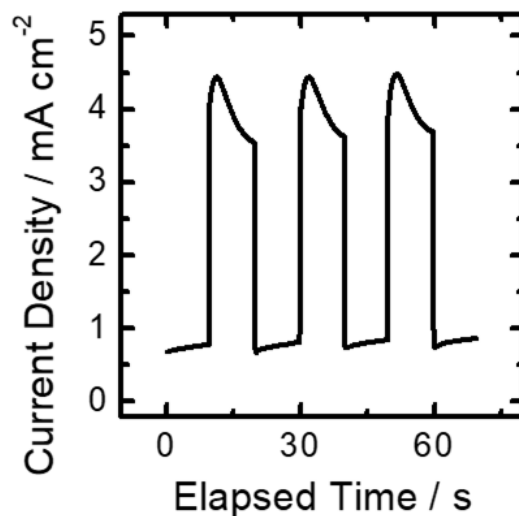
Spatially directed, inorganic phototropic growth of isolated Se-Te deposits can be generated in response to manipulation of the direction of a spatially conformal, incoherent, and unpolarized beam of light.<sup>46</sup> Se-Te has been electrochemically grown via cathodic electrodeposition from an aqueous solution of 0.020 M SeO<sub>2</sub>, 0.010 M TeO<sub>2</sub> and 2.00 M H<sub>2</sub>SO<sub>4</sub> under illumination on circular Au islands that were lithographically patterned onto an n<sup>+</sup>-Si substrate. The feature size and pitch of the Au islands were designed to minimize optical and electrochemical communication between adjacent regions of growth. Such isolation enabled investigation of the intrinsic material growth behavior independent of emergent phenomena, including array effects, which may dominate the growth characteristics of an unconstrained, extended film. Figure 1(a) and (b) present representative cross-sectional scanning-electron micrographs (SEMs) of isolated Se-Te deposits generated using a narrowband light-emitting diode (LED) source with an intensity-weighted average wavelength,  $\lambda_{\text{avg}}$ , of 528 nm, with the illumination incident at the indicated angle,  $\alpha$ , from the surface normal. With  $\alpha = 0^\circ$  (normal incidence, Figure 1.2(a)), a symmetrical, hemispherical cross-

section was observed. For  $\alpha = 60^\circ$  (Figure 1.2(b)), the deposit cross-section was somewhat hemispherical but exhibited marked asymmetry in that greater mass was observed on the side of the incident illumination relative to the opposite side.



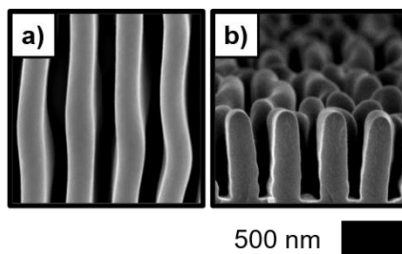
**Figure 1.3.** Simulated light absorption profiles in a model photoelectrodeposit morphology. Modeled using  $\lambda_{\text{avg}} = 528$  nm illumination incident at the indicated angle  $\alpha$  from the substrate normal.

To provide insight into the relation between the material absorption and the observed phototropic response, light absorption simulations were performed using full-wave electromagnetic simulations. Figure 1.3(a) and (b) presents graphical representations of the light absorption profiles calculated for the model structure using  $\lambda_{\text{avg}} = 528$  nm for  $\alpha = 0$  and  $60^\circ$ . For  $\alpha = 0^\circ$  (Figure 3a), the absorption profile was symmetrical and most of the absorption was strongly localized near the growth (solution) interface. With  $\alpha = 30^\circ$  (Figure 3b) the absorption was also tightly confined near the solution interface but was asymmetrically distributed spatially, with greater absorption on the side of the incident illumination. The extent of asymmetry in the absorption profiles correlated with the morphological anisotropies observed experimentally (Figure 1.2).



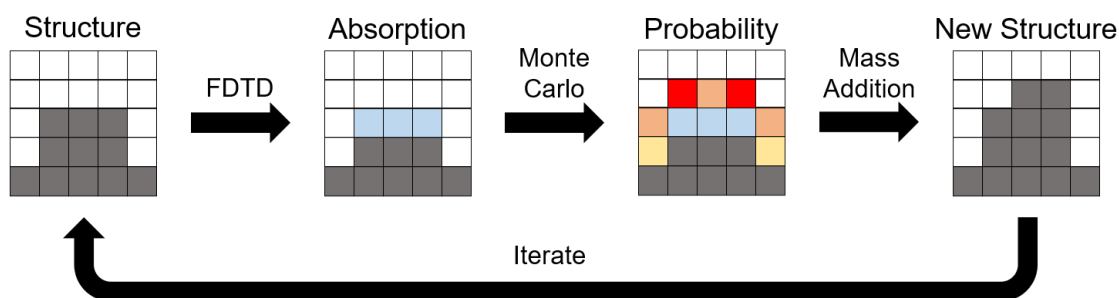
**Figure 1.4.** Chronoamperometry data for light-mediated cathodic Se-Te electrodeposition. Data acquired using a polarization of  $E = -0.400$  V vs. Ag/AgCl (3M) in a solution of 0.020 M SeO<sub>2</sub>, 0.010 M TeO<sub>2</sub>, 2.00 M H<sub>2</sub>SO<sub>4</sub> with  $\lambda_{\text{avg}} = 528$  nm illumination with a power of  $P = 14.5$  mW cm<sup>-2</sup> shuttered at 0.1 Hz.

Figure 1.4 presents chronoamperometry data for light-mediated Se-Te electrodeposition with shuttered illumination. The deposition current density is observed to be significantly higher under illumination than in the dark. This data, along with the light absorption simulations (Figure 1.3) indicate that the observed inorganic phototropic growth response (Figure 1.2) arises from spatially anisotropic absorption in the growing deposits, which in turn promotes locally elevated rates of electrochemical growth where absorption is high, resulting in directional growth.



**Figure 1.5.** Inorganic phototropic growth with an unpatterned substrate and unstructured illumination. (a) Top-down SEM representative of a Se-Te photoelectrodeposit generated with vertically polarized  $\lambda_{\text{avg}} = 955$  nm illumination. (b) Same as (a) but cleaved along the horizontal axis and acquired in cross-section.

Inorganic phototropic growth on unpatterned substrates using incoherent, uncorrelated illumination with spatially-invariant intensity can spontaneously generate films highly ordered, anisotropic mesostructures with nanoscale features over macroscale areas ( $\text{cm}^2$ ).<sup>47,48</sup> Such structures are formed without the use of a photomask or any physical or chemical templating agents.<sup>10,11,49-52</sup> Figure 1.5 presents a representative top-down SEM of a photoelectrodeposit generated via inorganic phototropic growth using vertically polarized  $\lambda_{\text{avg}} = 955$  nm illumination from an incoherent LED source. The SEM reveals a highly anisotropic lamellar morphology wherein the long axes of the lamellae are oriented parallel to the polarization axis. Figure 1.5(b) presents an analogous SEM to that in Figure 1.5(a) that was acquired in cross-sectional view from a sample that had been cleaved along the horizontal axis (perpendicular to the direction of polarization), providing a view down the lamellar axis and highlighting the high aspect ratio of the lamellar features and thus the substantial out-of-plane anisotropy of the photoelectrodeposit. Such template-free mesostructure growth demonstrates the capacity of inorganic phototropic growth to spontaneously generate defined nanoarchitectures.



**Figure 1.6.** Schematic summarizing the optically-based iterative growth model used to computationally assess inorganic phototropic growth. First, full-wave electromagnetic simulations using a finite-difference time-domain (FDTD) technique are performed to calculate the spatially-dependent light absorption profile. This is used to weight the probability of mass addition in a Monte Carlo routine. The process is then iterated to simulate continued growth.

Inorganic phototropism has been explored computationally using an optically-based, two-step iterative growth model that is graphically summarized in Figure 1.6. First, full-wave electromagnetic simulations are performed using a finite-difference time-domain method (FDTD) to determine the spatially dependent profile of light absorption at the growth interface. A Monte Carlo method is then used to add mass with a spatial probability weighted by the absorption calculated in the initial step. Empirical inputs were minimal and included estimates of the deposit complex refractive index and the electrolyte index.

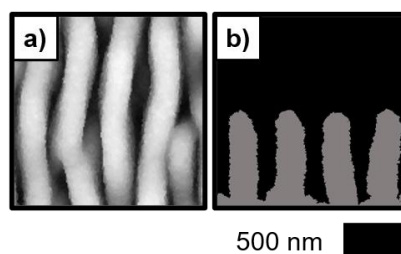


**Figure 1.7.** Simulated morphologies for inorganic phototropic growth with an unpatterned substrate and unstructured illumination. Se-Te growth modeled using vertically polarized  $\lambda_{\text{avg}} = 955 \text{ nm}$  illumination in (a) three dimensions and (b) two dimensions.

Figure 1.7 presents simulated morphologies analogous to the experimental data presented in Figure 1.5. Close agreement between the experimental and computational data indicates that the empirical structures are principally determined by optical processes as opposed to any (electro)chemical or crystallographic bias of the Se-Te material during growth.<sup>53-55</sup> Additionally, similar inorganic phototropic growth has been utilized to generate structures of crystalline PbSe and CdSe, and the same optically-based model used to simulate Se-Te growth successfully reproduced the morphologies of these materials with only the same set of limited empirical inputs.<sup>56,57</sup> These data demonstrate the generality of the process and suggest that it may be applied to direct the growth of a wide range of semiconductor materials. With such impetuses we began and now continue to explore the precise manner by which specific optical inputs result in precise mesoscale morphologies.<sup>58-62</sup>

### **1.3 Overview**

The following chapters explore the physical translation of defined optical excitation inputs into mesostructured morphological outcomes via inorganic phototropic growth and the underlying physical mechanisms. Chapter 2 provides the experimental and computational methods utilized in this investigation. Chapter 3 explores the response to the input wavelength and spectral distribution. Chapter 4 investigates control using linearly polarized inputs and Chapter 5 the expression of the relative phase and coherence of such inputs.

## *Chapter 2*

### METHODS

This chapter details the experimental and computational methods utilized to generate the data presented and discussed in the following chapters.

#### **2.1 Materials and Chemicals**

(CH<sub>3</sub>)<sub>2</sub>CO (ACS Grade, BDH), CH<sub>3</sub>OH (ACS Grade, EMD), H<sub>2</sub>SO<sub>4</sub> (ACS Reagent, J. T. Baker), HF (49 %, Semiconductor Grade, Puritan Products), In (99.999 %, Alfa Aesar), Ga (99.999 %, Alfa Aesar), SeO<sub>2</sub> (99.4 %, Alfa Aesar), and TeO<sub>2</sub> (99+ % Sigma-Aldrich) were used as received. H<sub>2</sub>O with a resistivity  $\geq 18.2$  M $\Omega$  cm (Barnstead Nanopure System) was used throughout. n<sup>+</sup>-Si(111) (0.004 – 0.006  $\Omega$  cm, As-doped, 400  $\pm$  15  $\mu$ m, single-side polished, Addison Engineering) was used as a substrate for deposition. Flash-Dry Silver Paint (SPI Supplies), Double/Bubble Epoxy (Hardman) and nitrocellulose-based nail polish were used to assemble the Si working electrodes.

## 2.2 Electrode Preparation

One end of a Sn-coated Cu wire (22 AWG) was bent to form a small, flat coil and the wire was then threaded through glass tubing (6 mm O. D.) such that the coil was just outside the tubing. Epoxy was applied to seal the end of the tube from which the coil protruded. Square Si wafer sections (ca. 5 mm by 5 mm) were cut and a eutectic mixture of Ga and In was scratched into the unpolished surfaces with a carbide scribe. The wire coil was then contacted to the unpolished surface and affixed with Ag paint. Nail polish was applied to insulate the unpolished face, as well as the wire-coil contact and the exposed wire between the coil and epoxy seal. Immediately before deposition, the Si surface of each electrode was cleaned with either  $(\text{CH}_3)_2\text{CO}$  alone or sequentially with  $(\text{CH}_3)_2\text{CO}$ ,  $\text{CH}_3\text{OH}$ , and  $\text{H}_2\text{O}$ , and then the Si section of the electrode was immersed in a 49 wt. % solution of  $\text{HF}(\text{aq})$  for  $\sim 10$  s, to remove any  $\text{SiO}_x$  present at the surface from the Si. The electrode was then rinsed with  $\text{H}_2\text{O}$ , and then dried under a stream of  $\text{N}_2(\text{g})$ .

### 2.3 Electrode Illumination

Illumination for the majority of the photoelectrochemical depositions was provided by narrowband diode (LED) sources (Thorlabs) with respective intensity-weighted  $\lambda_{\text{avg}}$  values and spectral bandwidths (FWHM) of 461 nm and 29 nm (M470L2), 630 nm and 18 nm (M625L2 or M625L3), 775 nm and 31 nm (M780L2), and 843 nm and 30 nm (M850L3). Additionally, a HeNe laser (Aerotech LSR5P) emitting at 632.8 nm in a TEM<sub>00</sub> mode with linear polarization, a broadband diode (LED, Thorlabs MBB1L3) with a relatively flat intensity profile between 500 and 750 nm ( $\lambda_{\text{avg}} = 646$  nm) and a spectral bandwidth (FWHM) of 280 nm, and an ELH-type tungsten-halogen lamp (Phillips 13096) with a  $\lambda_{\text{avg}}$  value of 640 nm and a spectral bandwidth (FWHM) of 420 nm, were also used as light sources.

The output of each diode source was collected and collimated with an aspheric condenser lens ( $\text{Ø}30$  mm,  $f = 26.5$  mm). The HeNe laser was fitted with a 10x beam expander (Melles-Griot) to create a spot that overfilled the working electrode. A dichroic film polarizer (Thorlabs LPVISE2X2 or LPNIRE200-B) was used to polarize the illumination from all the narrowband diode sources. Illumination from the broadband diode and from the tungsten-halogen lamp was polarized using an ultra-broadband wire-grid polarizer (Thorlabs WP25M-UB). For experiments involving simultaneous illumination with two sources with different  $\lambda_{\text{avg}}$  values, a dichroic filter (Edmund Optics #69-900 or #69-219) was utilized to combine the beam outputs. Both sources were incident upon a filter surface at an angle of 45 degrees from the surface normal, generating coaxial output. Similarly, for experiments involving simultaneous illumination with two  $\lambda_{\text{avg}} = 630$  nm sources, a polka dot beamsplitter

(Thor Labs BPD508-G) was utilized in the same geometry to combine the outputs. For experiments involving simultaneous illumination with a  $\lambda_{\text{avg}} = 630$  nm source along with either a  $\lambda_{\text{avg}} = 461$  nm or  $\lambda_{\text{avg}} = 843$  nm source, a single polarizer was placed after the dichroic filter to ensure that all the light that reached the electrode shared a single polarization vector. For experiments involving simultaneous illumination with a  $\lambda_{\text{avg}} = 630$  nm source along with either another  $\lambda_{\text{avg}} = 630$  nm source or a  $\lambda_{\text{avg}} = 775$  nm sources, a polarizer was placed between each source and the appropriate combining optic, to enable independent control of the polarization of each source. No polarizer was used in conjunction with the HeNe laser. For experiments using a series of elliptical polarization states, the output from the HeNe laser was directed at normal incidence through a zero-order  $\lambda/4$  plate (Thorlabs WPQ10E-633). The  $\lambda/4$  plate was rotated about the optical axis such that the fast axis of the plate was oriented at angles between 0 and 45° clockwise from the polarization axis of the laser. The presence of the  $\lambda/4$  plate generated a  $\phi = 90^\circ$  phase angle between the orthogonal components of the laser illumination and provided for the generation of defined elliptical polarization. For all experiments, a 1500 grit ground-glass (N-BK7) diffuser was placed immediately in front of the photoelectrochemical cell to ensure spatial homogeneity of the illumination.

The light intensity incident on the electrode was measured by placing a calibrated Si photodiode (Thorlabs FDS100) in the place of an electrode assembly in a photoelectrochemical cell with electrolyte, and measuring the steady-state current response of that Si photodiode. Depositions that utilized a single diode with  $\lambda_{\text{avg}} = 461$  nm or  $\lambda_{\text{avg}} = 646$  nm as the illumination source were performed with a light intensity

of  $25.0 \text{ mW cm}^{-2}$  at the electrode. Depositions with the HeNe laser were performed with a light intensity of  $10.0 \text{ mW cm}^{-2}$  for the experiment described in Chapter 2 and  $13.7 \text{ mW cm}^{-2}$  for experiments described in Chapter 4. Depositions with the tungsten-halogen lamp were performed with a light intensity of  $50.0 \text{ mW cm}^{-2}$ . Depositions using a single  $\lambda_{\text{avg}} = 630 \text{ nm}$  source were performed with a light intensity of  $25.0 \text{ mW cm}^{-2}$  for the experiments described in Chapter 2 and  $13.7 \text{ mW cm}^{-2}$  for the experiments described in Chapters 3 and 4. Depositions utilizing a  $\lambda_{\text{avg}} = 630 \text{ nm}$  source in conjunction with a  $\lambda_{\text{avg}} = 461 \text{ nm}$  source, another  $\lambda_{\text{avg}} = 630 \text{ nm}$  source, a  $\lambda_{\text{avg}} = 775 \text{ nm}$  source, or a  $\lambda_{\text{avg}} = 843 \text{ nm}$  source, simultaneously were performed with total light intensities of 25.0, 13.7, 30.0, and  $50.0 \text{ mW cm}^{-2}$ , respectively.

## 2.4 Photoelectrochemical Deposition

Photoelectrochemical deposition was performed using a Bio-Logic SP-200 potentiostat. Deposition was performed in a single-compartment glass cell with either a pyrex or quartz window. A three-electrode configuration was utilized with a graphite-rod counter electrode (99.999 %, Sigma-Aldrich) and a Ag/AgCl reference electrode (3 M KCl, Bioanalytical Systems). Films were deposited from an aqueous solution of 0.0200 M SeO<sub>2</sub>, 0.0100 M TeO<sub>2</sub> and 2.00 M H<sub>2</sub>SO<sub>4</sub>. Deposition was effected by biasing the illuminated n<sup>+</sup>-Si electrode potentiostatically at -0.40 V vs. Ag/AgCl for 5.00 min at room temperature. After deposition, the electrode was immediately removed from the cell, rinsed with H<sub>2</sub>O, and then dried under a stream of N<sub>2</sub>(g). The Si substrate with a top-facing Se-Te film was mechanically separated from the rest of the electrode assembly. The nitrocellulose-based insulation, as well as the majority of the Ag paint and In-Ga eutectic, were then removed mechanically.

## 2.5 Scanning-Electron Microscopy

Scanning-electron micrographs (SEMs) were obtained with a FEI Nova NanoSEM 450 at an accelerating voltage of 5.00 kV with a working distance of 5 mm and an in-lens secondary electron detector. Micrographs obtained for quantitative analysis were acquired with a resolution of 172 pixels  $\mu\text{m}^{-1}$  over ca. 120  $\mu\text{m}^2$  areas. Micrographs utilized to produce display figures were acquired with a resolution of 344 pixels  $\mu\text{m}^{-1}$  over ca. 8  $\mu\text{m}^2$  areas.

## 2.6 Iterative Growth Modeling

The growths of the photoelectrochemically deposited films were simulated with an iterative growth model wherein electromagnetic simulations were first used to calculate the local photocarrier-generation rates at the film surface. Then, mass addition was simulated via a Monte Carlo method wherein the local photocarrier-generation rate weighted the local rate of mass addition along the film surface.

Growth simulations began with a bare, semi-infinite planar Si substrate. In the first step, the light-absorption profile under a linearly polarized, plane-wave illumination source was calculated using full-wave finite-difference time-domain (FDTD) simulations (“FDTD Solutions” software package, Lumerical) with perfectly matched layer boundary conditions imposed in the direction normal to the substrate and periodic boundary conditions imposed in the orthogonal direction(s). In the second step, a Monte Carlo simulation was performed in which an amount of mass, equaling that of a 10 nm (for simulations presented in Chapters 2 and 4) or 15 nm (for the simulations presented in Chapter 3) planar layer that covered the simulation area, was added to the upper surface of the structure with a probability  $F$ :

$$F(G) = G \prod_{i=1}^3 \frac{x_i}{r_i} \quad (\text{Equation 1})$$

where  $G$  is the spatially dependent photocarrier-generation rate at the deposit/solution interface,  $x_i$  is the fraction of  $i^{\text{th}}$  nearest neighbors occupied in the cubic lattice, and  $r_i$  is the distance to the  $i^{\text{th}}$  nearest neighbor. The multiplicative sum in the definition of this probability (Equation 1) serves to reduce the surface roughness of the film so as to mimic the experimentally observed surface roughness. After the initial Monte Carlo

simulation, the absorbance of the new, structured film was then calculated in the same manner as for the initial planar film, and an additional Monte Carlo simulation of mass addition was performed. This process of absorbance calculation and mass addition was repeated for a total of 30 iterations for the simulations described in Chapters 2 and 3 and for 20 iterations for the simulation described in Chapter 4.

A value of  $n = 1.33$  was used for the refractive index of the electrolyte regardless of wavelength.<sup>63</sup> Previously measured values of the complex index of refraction for Se-Te were utilized.<sup>47</sup> Illumination intensities identical to those used experimentally (see above) were used in the simulations. The electric field vector of the illumination was oriented parallel to the substrate.

## **2.7 Simulation of Field Amplitude Resulting from Dipole Emitters**

The time-averaged field amplitude resulting from two coherent dipole sources was calculated using two-dimensional FDTD simulations (“FDTD Solutions” software package, Lumerical). For simulations representing two illumination sources with different polarizations, the field amplitude profile was rotated about the simulation center and summed with the original field amplitude. A two-dimensional square simulation mesh with a lattice constant of 14 nm was used.

## 2.8 Simulation of Absorption in Idealized Structures

Three-dimensional FDTD simulations (“FDTD Solutions” software package, Lumerical) were used to calculate the normalized absorption profile of two intersecting idealized lamellar structures. A three-dimensional cubic simulation mesh with a lattice constant of 2 nm was used. The idealized structure, from bottom to top, consisted of a semi-infinite Si substrate, a 100 nm conformal Se-Te layer, and two Se-Te lamellae with hemispherical upper boundaries. The lamellae were either 200 nm or 400 nm tall as indicated in Chapter 4, as measured from the upper boundary of the conformal layer.

## Chapter 3

### SELF-OPTIMIZING PHOTOELECTROCHEMICAL GROWTH OF NANOPATTERNED SE-TE FILMS IN RESPONSE TO THE SPECTRAL DISTRIBUTION OF INCIDENT ILLUMINATION

Carim, A. I.; Batara, N. A.; Premkumar, A.; Atwater, H. A.; Lewis, N. S. *Nano Letters*, **2015**, *15*, 7071-7076. DOI: 10.1021/acs.nanolett.5b03137

#### **3.1 Introduction**

In this chapter, we describe the relationship between the morphologies of photoelectrodeposited Se-Te films and the spectral profiles of the illumination utilized during the growth of the films. Deposition was performed in the presence of an array of narrowband, broadband, and multi-modal illumination profiles, respectively, to determine the morphology produced by changes in the properties of the optical excitation. Fourier analysis was utilized to provide a quantitative description of the patterns, and the patterns were accurately reproduced by computational modeling and simulation of the light-material interactions during growth of the films.

### 3.2 Results and Discussion

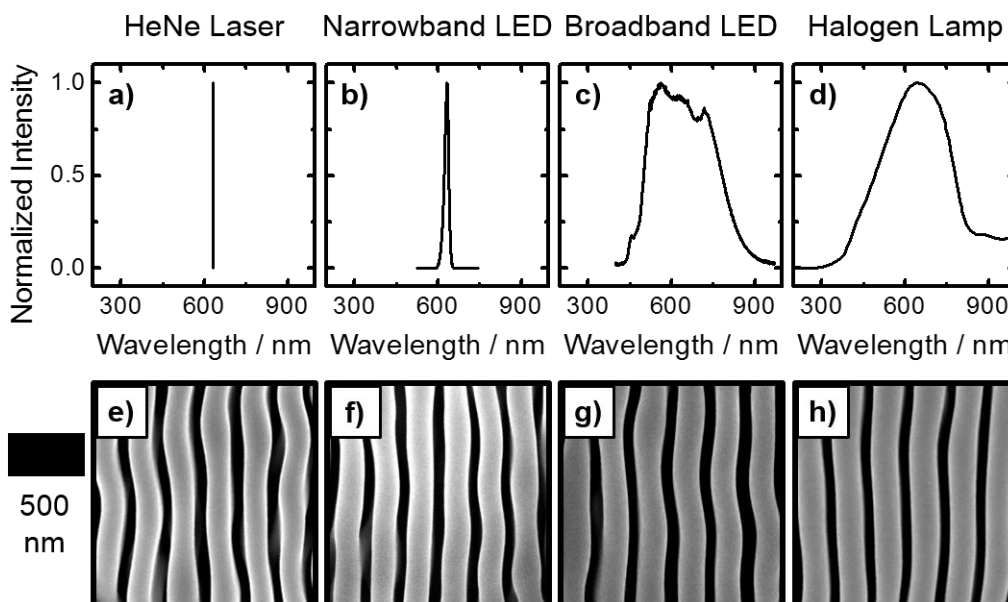


**Figure 3.1.** Effect of the spectral bandwidth of vertically polarized illumination sources on the morphology of photoelectrodeposited Se-Te films. (a)-(d) Spectral profiles for indicated sources. (e)-(h) Corresponding scanning electron micrographs representative of the resulting photoelectrodeposited films.

Se-Te photoelectrodeposits produced by illumination with polarized, narrowband coherent or incoherent light between  $450 < \lambda < 950$  nm form lamellae that are aligned along the optical polarization direction, with a periodicity proportional to the incident optical wavelength. Figure 3.1(a)-(d) presents spectral profiles of four light sources that had very similar intensity-weighted average wavelengths ( $\lambda_{\text{avg}}$ ) but had very different spectral bandwidths: a HeNe laser with  $\lambda_{\text{avg}} = 633$  nm and a bandwidth (full-width at half-max, FWHM)  $\ll 1$  nm; a narrowband light-emitting diode (LED) with  $\lambda_{\text{avg}} = 630$  nm and FWHM = 18 nm; a broadband LED with  $\lambda_{\text{avg}} = 646$  nm and FWHM = 283 nm; and a tungsten-halogen lamp with  $\lambda_{\text{avg}} = 640$  and FWHM = 420

nm. Figure 3.1(e)-(h) presents representative scanning-electron micrographs (SEMs) of photoelectrodeposits generated by the potentiostatic electrochemical reduction of  $\text{SeO}_2$  and  $\text{TeO}_2$  under illumination with each separate, vertically polarized light source. The Se-Te films exhibited mutually similar morphologies regardless of which illumination source was utilized (Figure 3.1). These morphologies are similar to ripple patterns that are generated using laser surface processing, known as laser-induced periodic surface structures (LIPSS).<sup>64-66</sup> However, formation of LIPSS requires coherent, highly monochromatic, and extremely intense (typically at  $\text{kW cm}^{-2}$  or  $\text{MW cm}^{-2}$  scales) laser excitation, whereas none of the illumination sources utilized in this investigation had all of these qualities.<sup>67,68</sup> Moreover, the broadband LED and halogen lamps produced light that was incoherent and highly polychromatic, with intensities on the order of  $\text{mW cm}^{-2}$ . Thus, it is apparent that a distinct mechanism must control the pattern formation in the system considered herein.

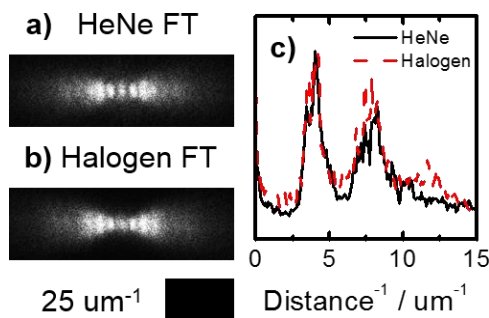


**Figure 3.2.** Fourier analysis of film morphologies generated with narrowband and broadband spectral distributions yielding a similar intensity-averaged wavelength. (a) and (b) Representative 2D Fourier transforms generated from SEMs of the films photoelectrodeposited using the indicated sources. (c) Fourier spectra generated by integrating the grayscale intensity along a narrow band starting at the center and extending out along the horizontal axis of the Fourier images presented in (a) and (b).

Figure 3.2(a) and (b) present two-dimensional Fourier transforms (2D FTs) of the SEM data of the photoelectrodeposited films using the HeNe laser and the tungsten-halogen lamp, respectively. A bright spot in a 2D FT corresponds to a periodic component in the SEM from which the 2D FT was derived. Moreover, in a 2D FT, the distance of any spot from the center indicates the frequency of the component, and the relative location indicates the direction of the periodicity. Thus the spots along the horizontal axes in Figure 3.2(a) and (b) are indicative of horizontal periodicity in the SEMs of the deposit morphologies. The similarity between the 2D FTs suggests that similar periodicities of the lamellar morphologies were generated with both the laser and the lamp. By integrating the grayscale intensity along a narrow band starting at the center and extending out along the horizontal axis of the 2D FT, a Fourier spectrum was generated to enable quantitative analysis of the data. Figure 3.2(c) presents Fourier spectra corresponding to the 2D FTs in Figure 3.2(a) and (b).

The extremely close agreement between the Fourier spectra describing the morphologies generated with the laser and lamp indicates a very similar periodic nature of these two morphologies despite a difference of several orders of magnitude between the bandwidths of the two sources.

The inverse of the lowest frequency maximum in each Fourier spectrum was equal to the lamellar periodicity (i.e. distance between identical points on two neighboring lamellae). The higher frequency maxima were integral multiples of the lowest maximum, and thus simply represent overtones of a fundamental frequency. The presence of overtones at higher frequencies is expected because the shapes of the lamellae are not perfectly described by a single sinusoidal function. The lack of any other components beyond a singular set of harmonics suggests that each morphology can be well-described by a single period. Thus despite the broadband source providing photons with widely differing excitation wavelengths, only a singular morphological periodicity was produced, exactly as is observed when a single periodicity results from a laser source that instead provides photons having only an extremely narrow distribution of wavelengths. Quantitatively, the real-space lamellar periodicity determined from the Fourier spectra was  $245 \pm 4$  nm for deposits generated with the laser and  $250 \pm 3$  nm for the lamp based on at least 5 independent measurements of each type of sample. Similar analysis of the deposits generated with LED sources resulted in a value of  $244 \pm 4$  nm for the narrowband LED and  $252 \pm 8$  nm for the broadband LED, again based on at least 5 independent measurements of each type of sample.

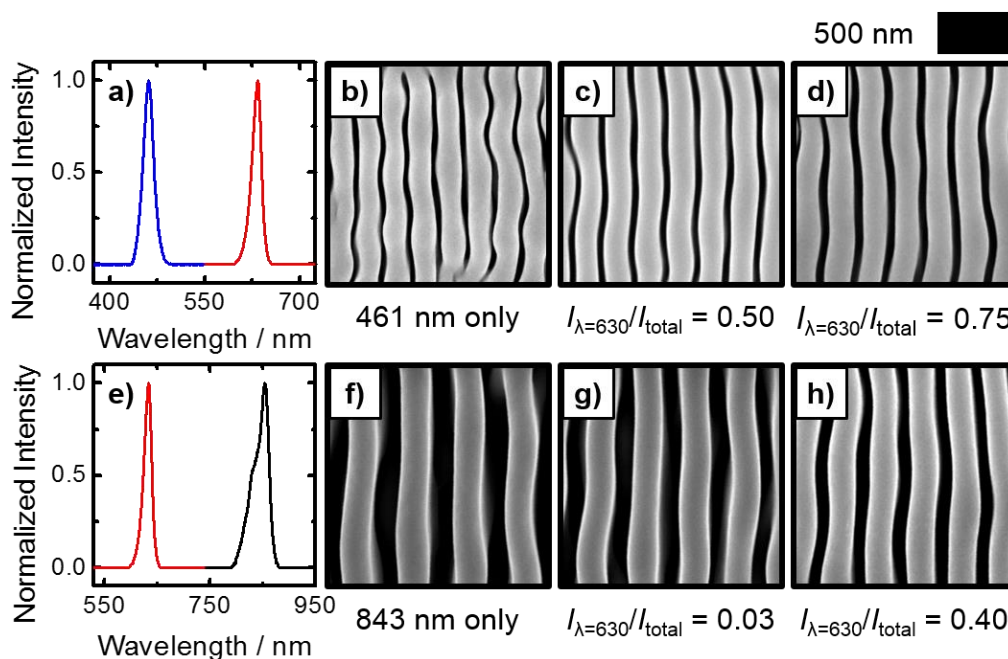


**Figure 3.3.** Effect of simultaneous illumination with two discrete narrowband sources on the morphology of photoelectrodeposited Se-Te films. (a) Spectral profile of the photoelectrodeposited Se-Te films. (a) Spectral profile of the illumination resulting from the combination of two narrowband LED sources with  $\lambda_{\text{avg}}$  values of 461 nm and 630 nm (at an arbitrary intensity ratio). (b)-(d) SEMs representative of the photoelectrodeposits resulting from illumination with a similar spectral profile as in (a) with the indicated intensity ratio between the two sources. (e)-(h) Same as (a)-(d), but with a source with a  $\lambda_{\text{avg}}$  value of 843 nm rather than 461 nm.

Collectively, the results obtained with the sources of varying bandwidths indicate that the lamellar periodicity is determined by an effective average source wavelength. This concept was investigated further by performing the photoelectrodeposition with spectral profiles that produced an intensity-weighted average spectral wavelength at a value at which the source had no actual intensity. Such profiles were obtained by simultaneously illuminating the sample with two narrowband LED sources. Figure 3.3(a) presents the spectral profile that resulted from illumination

with a narrowband LED with  $\lambda_{\text{avg}} = 630$  nm in conjunction with illumination from another narrowband LED having  $\lambda_{\text{avg}} = 461$  nm. Figure 3.3(b) presents a SEM of a deposit generated with only 461 nm illumination and Figure 3.3(c) and (d) presents SEMs of deposits generated with simultaneous illumination at 461 nm and 630 nm, as a function of the fraction of the total delivered intensity that was provided by each narrowband light source. The SEMs observed from a deposit generated using 461 nm illumination displayed a smaller lamellar periodicity than was observed for the corresponding deposit grown using 630 nm illumination. Deposits generated using illumination with both wavelengths appeared to display intermediate periodicities. Figure 3.3(e)-(f) presents analogous data, but with an LED having  $\lambda_{\text{avg}} = 843$  nm rather than 461 nm. As noted in the experiment using 461 nm and 630 nm sources, the deposition under illumination with the longer wavelength source alone generated what appeared to be the largest periodicity, while deposits formed under illumination by both sources simultaneously resulted in lamellar periods intermediate between those observed for deposition with either source alone.

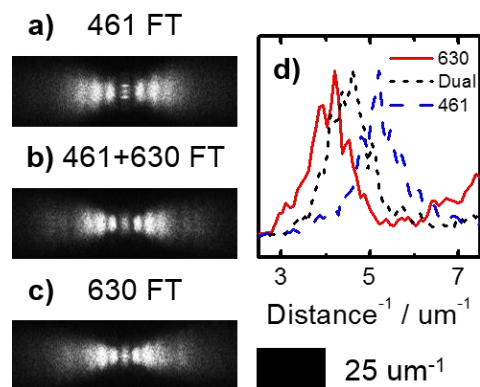


**Figure 3.4.** Fourier analysis of film morphologies generated with single and multimodal spectral distributions. Representative 2D Fourier transforms of SEMs of photoelectrodeposits generated using (a) a single narrowband source with a  $\lambda_{\text{avg}}$  value of 461 nm, (b) two narrowband sources with  $\lambda_{\text{avg}}$  values of 461 nm and 630 nm, and (c) a single narrowband source with a  $\lambda_{\text{avg}}$  value of 630 nm. (d) Fourier spectra generated by integrating the grayscale intensity along a narrow band starting at the center and extending out along the horizontal axis of the Fourier images presented in (a)-(c).

Fourier analysis was also used to analyze the periodicity of the patterns in the photoelectrodeposits grown using simultaneous illumination from two narrowband sources. Figure 3.4(a)-(c) presents 2D FTs of SEMs of deposits generated with illumination provided by the 461 nm source alone, the 461 and 630 nm sources together, and the 630 nm source alone. Each 2D FT displayed discrete bright spots along the horizontal axis, and the spacing of these spots was the greatest in the 2D FT of the 461 nm sample and smallest in the 2D FT of the 630 nm sample. The spacing in the 2D FT of the dual-wavelength sample was intermediate between the spacings for the 461 nm and 630 nm samples. In all three cases, the corresponding Fourier spectra generated from integration of these three 2D FTs revealed that the only observable components were a fundamental mode and corresponding overtones.

Figure 3.4(d) presents the corresponding Fourier spectra in the region of the fundamental. The fundamental peak in each spectrum was centered at a different value along the abscissa, and the center of the dual-wavelength peak was intermediate between the centers of both related single-wavelength peaks. Thus, under the conditions investigated, photoelectrochemical growth with two discrete narrowband sources resulted in a deposit that had only a single characteristic morphological period, and had no detectable beat frequencies in contrast to expectations based on simple interference.

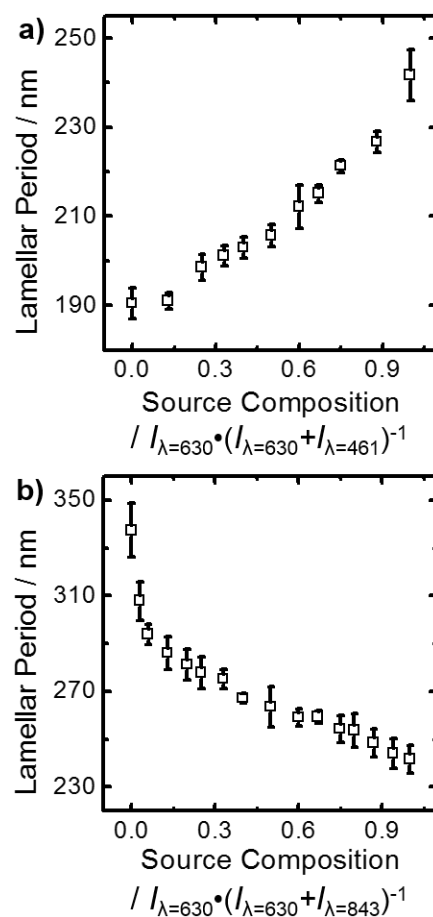


**Figure 3.5.** Photoelectrodeposit lamellar period as a function of the fraction of the total, two-source intensity provided by a 630 nm source utilized during growth.

Figure 3.5(a) presents a plot of the lamellar period derived from the 2D FTs of SEMs of photoelectrodeposits generated with simultaneous illumination at 461 nm and 630 nm as a function of the source composition. Figure 3.5(b) presents analogous data characteristic of photoelectrodeposits generated with 630 nm and 843 nm illumination. In both cases, the lamellar periods observed for photoelectrodeposits generated using simultaneous illumination with two different wavelengths were intermediate between those observed for photoelectrodeposits generated with either

one of the two constituent wavelengths alone. Also, in both cases, the lamellar period scaled monotonically between these limits as a function of source composition, in an inverse logistic-like curve. Such behavior has several implications. First, by utilization of two sources with differing wavelengths, a structure with any period between the limits defined by the periods observed for growth with either source alone can be generated simply by varying the relative intensity of the two sources. Second, under such conditions, the growth is sensitive to the characteristics of both sources, because the lamellar period reflected the engineered spectral profile of the illumination under every condition investigated. In fact, near the extremes of the source composition, wherein one source supplied the majority of the intensity, the lamellar period was generally the most sensitive to a change in source composition.

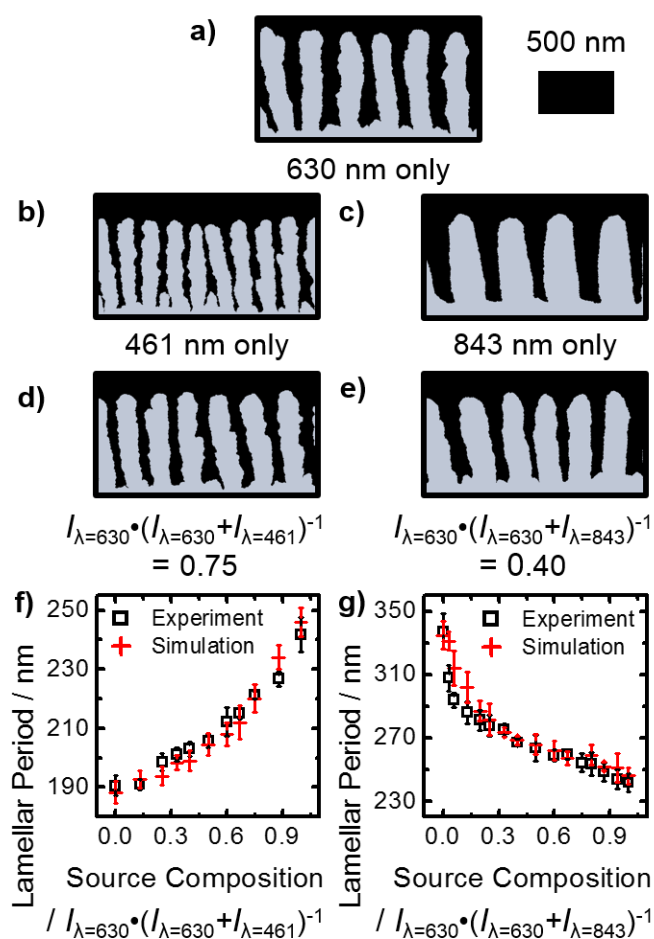


**Figure 3.6.** Computational growth modeling data representative of photoelectrodeposited Se-Te film morphologies generated using simultaneous illumination with two discrete narrowband sources. (a)-(e) 2D simulations of photoelectrodeposits generated with indicated illumination source(s). (f) and (g) Plots of lamellar period of the experimental and simulated photoelectrodeposit morphologies as a function of the fraction of the total, two-source intensity provided by a 630 nm source utilized during growth/modeling.

Modeling of the photoelectrochemical growth process was performed to determine if the morphologies observed for films generated using simultaneous illumination with narrowband sources evolved as a result of the fundamental light-matter interactions that occurred during the deposition. The two-step, iterative model

described in Chapter 1 was utilized wherein electromagnetic simulations were first used to calculate the local photocarrier-generation rates at the electrode/solution interface and then electrochemical addition of mass was simulated via a Monte Carlo method that utilized the local photocarrier-generation rate to weight the local probabilities of mass. Figure 3.6(a), (b), and (c), respectively, present 2D simulations (cross-sectional view) of the morphologies of photoelectrodeposits generated using illumination at 630 nm, 461 nm, and 843 nm alone. The morphological periodicity in each presented simulation was in good agreement with that observed experimentally (Figure 3.1(f), Figure 3.3(b) and (f)). Figure 3.6(d) and (e) present 2D simulations of the morphologies of photoelectrodeposits generated with illumination at 630 nm simultaneously with illumination at either 461 nm or 843 nm, respectively. In both cases, the simulated morphologies displayed periodicities that were intermediate between those observed in the simulations of morphologies generated under illumination with either of two sources alone. Moreover, the simulated morphologies were in good agreement with those observed experimentally (Figure 3.3(d) and (h)). Thus, the modeling and simulation agreed qualitatively with the experimental data.

The lamellar period in the simulated structures was derived from FT analysis, in an analogous fashion to analysis of the structures that were observed experimentally (Figure 3.2). Figure 3.6(f) presents the lamellar period of the morphologies of the simulated photoelectrodeposits, as well as the corresponding experimental morphologies, for growth under simultaneous illumination with 461 nm and 630 nm sources as a function of source composition. Figure 3.6(g) presents analogous data characteristic of simulations and photoelectrodeposits that were obtained by

simultaneous use of 630 nm and 843 nm illumination. The experimental and simulated values of the lamellar period matched quantitatively in both cases. Such quantitative agreement between the model and experiment indicates that any arbitrary illumination profile during growth encodes for a singular lamellar period. Additionally, the specific period appears spontaneously in the photoelectrodeposit due only to the interactions between the illumination and the evolving deposit during growth.

The generation of the highly anisotropic, periodic lamellar pattern is directly the result of highly differing rates of mass addition along the film surface. Specifically, to perpetuate the morphological asymmetry, the local growth rate must be greatest at the tip of the lamellar surface. Light absorption provides the driving force in the modeling for photoelectrochemical deposition, hence the success of the iterative growth model in reproducing the observations indicates that generation of the periodic lamellar pattern requires the absorption of light to be greatest in the tips of the lamellar structure and less than maximal in areas other than the tips of the structure. The experimental results and growth model also collectively indicated that a lamellar pattern having a single periodicity is always formed under the conditions investigated, regardless of the spectral profile of the illumination. Collectively, the experiments and simulations suggest that for a given illumination profile, the photoelectrodeposition process spontaneously self-selects the lamellar period that will maximize light absorption at the tips of the lamellar structures. A set of light-absorption simulations were performed considering an idealized lamellar structure to verify that the experimentally observed periods were those that maximized the anisotropy of the light absorption.

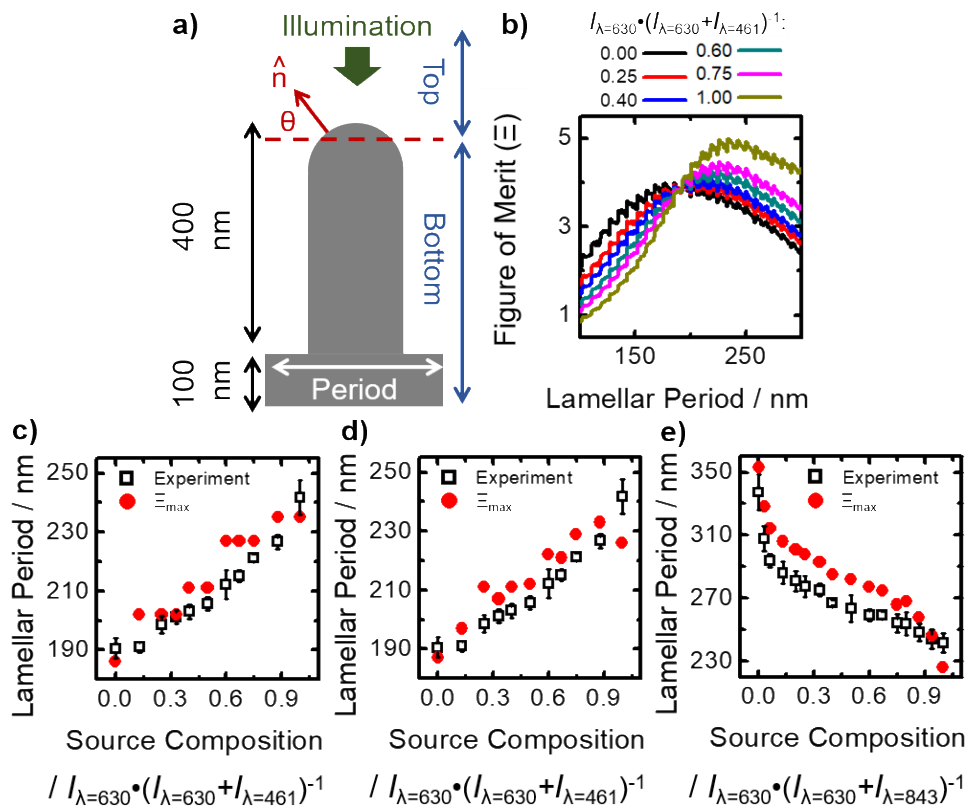


**Figure 3.7.** Computational analysis of light absorption anisotropy in idealized lamellar structures under simultaneous illumination with two discrete narrowband sources. (a) Diagram of the simulation area containing an idealized lamellar structure utilized for calculations of the spatial concentration of light absorption. The lamella was divided into top and bottom segments at the height at which the surface normal of the tip ( $\hat{n}$ ) was at an angle  $\theta = 45$  degrees from the horizontal. Plane-wave illumination was incident from the top of the structure, with a propagation oriented normal to the substrate. (b) Plots of figure of merit,  $\Xi$ , or light absorption in the top surface of the idealized structure normalized by that in the bottom, as a function of lamellar period for simultaneous illumination at 461 nm and 630 nm with the indicated source composition. (c) Plot of the experimentally observed lamellar period and the lamellar period which maximized  $\Xi$  as a function of the fraction of the total intensity provided by the 630 nm source utilized during growth/modeling. (d) and (e) Same as (c) but based on simulations utilizing a finer discretization of the lamellar structure.

Figure 3.7(a) provides a schematic for the simulation area that contained the idealized structure, consisting of a 400 nm tall lamella that had a hemispherical upper bound atop a 100 nm conformal layer of the electrodeposit. The width of structures in the simulations was set as the product of the lamellar period and the empirically derived filling fraction for the illumination condition under analysis (quantified by contrast-thresholding the same SEMs utilized for Fourier analysis). The illumination was simulated to be incident with a propagation vector parallel to the lamellar tip. Periodic boundary conditions were used to simulate an array of lamellae. The structure was considered as two segments, “top” and “bottom”, with the boundary between the two segments located at the height at which the surface normal of the tip was 45 degrees from horizontal. A figure of merit,  $\Xi$ , was defined as the ratio of absorbed photons in the interfacial region of the top versus that of the bottom. A figure of merit,  $\Xi$ , was defined as the ratio of number of absorbed photons at the top solid/solution interface to the number of absorbed photons at the bottom solid/solution interface. The value of  $\Xi$  was thus proportional to the degree of light concentration in the top of the lamellar structure. Calculation of  $\Xi$  was limited to photons that were absorbed within 10 nm of the interface.

For a given illumination profile,  $\Xi$  was calculated over a series of lamellar periods ranging from 100 to 400 nm. Figure 3.7(b) illustrates the dependence of  $\Xi$  on the lamellar period for simultaneous illumination at 461 nm and 630 nm with several experimentally investigated source compositions. Each  $\Xi$ -curve had a single maximum, which shifted to a larger value of the lamellar period for illumination profiles as the 630 nm content of the illumination increased. Figure 3.7(c) presents a plot of the lamellar

period at  $\Xi_{\max}$  for simulations involving simultaneous illumination at 461 nm and 630 nm, as a function of the source composition. The experimentally observed values are also presented in Figure 3.7(c). The stair-step shape of the  $\Xi$ -derived curve is an artifact that arose because the simulations considered the structure as many finite, but insufficiently small, units. Identical simulations that instead involved smaller units exceeded the available computational resources. Nevertheless, the values of the lamellar period that maximized  $\Xi$  matched semi-quantitatively with the analogous experimental values. To accommodate computational limitations while improving the accuracy of the model,  $\Xi$  was recalculated with simulations that utilized a finer discretization of the structure, but only was performed in a narrow range of lamellar periods near the previously observed maxima (using the coarser discretization), for every experimentally investigated source composition. Figure 3.7(d) presents the derived plot of the lamellar period at the new values of  $\Xi_{\max}$ , along with the related experimental data. Figure 3.7(e) presents an analogous plot for simultaneous illumination with 630 nm and 843 nm. The lamellar periods that maximized  $\Xi$  followed the same trend with respect to source composition as the experimentally measured periods, and the two sets of values matched essentially quantitatively. The agreement between the experimental data and the simulations indicates that the observed photoelectrochemical growth spontaneously optimized the lamellar period in a way that maximized the anisotropy of the light absorption.

### 3.3 Conclusions

In summary, under the conditions investigated, photoelectrochemical deposition utilizing linearly polarized illumination has been shown to result spontaneously in an ordered nanoscale lamellar morphology, regardless of the wavelength distribution of the illumination source. Fourier analysis demonstrated that this morphology was consistently described by only a single periodicity. Utilization of several illumination profiles with different bandwidths but having a common intensity-weighted average wavelength resulted in structures that had a mutually common, singular periodicity. Similarly, illumination profiles that consisted of two narrowband sources generated structures that had singular periodicities which were a function of the relative contribution of each source to the total illumination intensity. Simulation of the growth process with such illumination spectral profiles showed that this phenomenon could be described by considering only the fundamental light-matter interactions that govern the photoelectrochemical growth process. Further simulations of light absorption under the same illumination profiles indicated that the photoelectrodeposition process is consistent with a self-optimization process that maximizes the anisotropy of light absorption in the structure along the growth front.

## Chapter 4

### POLARIZATION CONTROL OF MORPHOLOGICAL PATTERN ORIENTATION DURING LIGHT-MEDIATED SYNTHESIS OF NANOSTRUCTURED SE-TE FILMS

Carim, A. I.; Batara, N. A.; Premkumar A.; Atwater, H. A.; Lewis, N. S. *ACS Nano*, **2016**, *10*, 102-111. DOI: 10.1021/acs.nano.5b05119

#### 4.1 Introduction

In this chapter, we investigate the patterns generated in photoelectrochemically grown Se-Te films utilizing two light sources with unique linear polarizations to understand the material growth response to the tailored excitation, as well as to identify strategies for obtaining morphology control and for generating three-dimensional morphological complexity. Films were generated using two same-wavelength sources with an array of polarization vector pairs as well as intensity ratios, and with two orthogonally polarized different-wavelength sources that had a series of intensity ratios. Computational modeling of the light-material interactions during photoelectrochemical growth successfully reproduced experimentally observed morphologies. Additional modeling of light scattering at the active film-solution interface, as well as simulations of light absorption idealized lamellar arrays, were also performed to understand the emergence of the morphologies generated using two discrete linear polarizations of light to drive film growth.

## 4.2 Results and Discussion

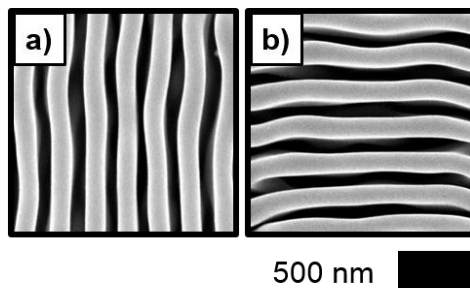


**Figure 4.1.** Effect of illumination source polarization on orientation of photoelectrodeposit morphology. SEMs representative of photoelectrodeposits generated with  $\lambda_{\text{avg}} = 630$  nm illumination polarized (a) vertically and (b) horizontally.

Figure 4.1 presents representative SEMs of Se-Te photoelectrodeposits generated using illumination with a narrowband LED with  $\lambda_{\text{avg}} = 630$  nm polarized vertically (a) and horizontally (b). In both cases, a highly anisotropic, lamellar-type morphology was observed. The long axis of the lamellar structures was oriented parallel to the polarization of the illumination; hence, vertical polarization resulted in vertically oriented lamellae whereas horizontal polarization yielded horizontally oriented lamellae.

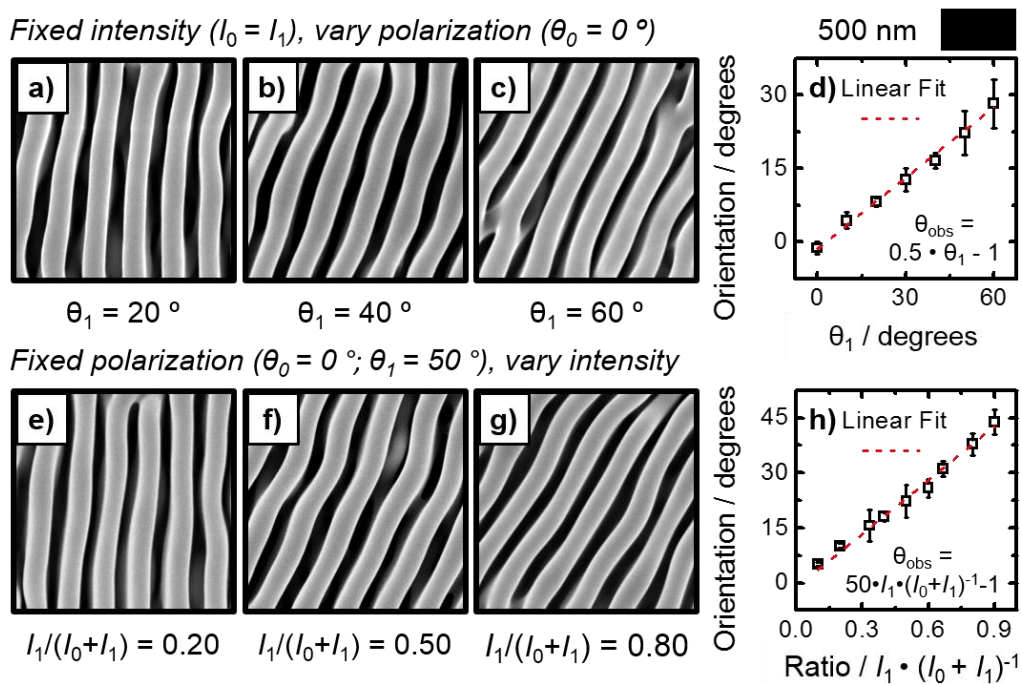


**Figure 4.2.** Orientation of photoelectrodeposit morphologies generated using two same-wavelength sources with differing linear polarizations. (a)-(c) SEMs representative of photoelectrodeposits generated using two  $\lambda_{\text{avg}} = 630$  nm sources with equal intensity, the first source polarized vertically ( $\theta_0 = 0^\circ$ ) and the second at the indicated rotation ( $\theta_1$ ) clockwise from the vertical. (d) Plot of the rotation of the orientation of the long axis of the pattern ( $\theta_{\text{obs}}$ ) measured clockwise from the vertical as a function of  $\theta_1$ . (e)-(g) SEMs representative of photoelectrodeposits generated using two  $\lambda_{\text{avg}} = 630$  nm sources, each with a fixed linear polarization (the first polarized vertically, the second offset  $\theta_1 = 50^\circ$  clockwise from the vertical) with the indicated fraction of the total intensity supplied by the second source [ $I_1 / (I_0 + I_1)$ ]. (h) Plot of  $\theta_{\text{obs}}$  as a function of the fraction of the total intensity supplied by the second source.

Figure 4.2(a)-(c) presents SEMs representative of photoelectrodeposits generated using two equal intensity LED sources with  $\lambda_{\text{avg}} = 630$  nm. One source was polarized vertically and the polarization of the second source was offset clockwise from the vertical by  $\theta_1 = 20^\circ$  (a),  $40^\circ$  (b), or  $60^\circ$  (c). In each case, a lamellar pattern

was observed that was similar to the pattern produced when only a single source was utilized. The long axis of the lamellar structures rotated clockwise away from the vertical in each case, and the magnitude of this rotation ( $\theta_{\text{obs}}$ ) increased with increasing values of  $\theta_1$ . For  $\theta_1 = 20^\circ$ ,  $40^\circ$ , and  $60^\circ$ , values of  $\theta_{\text{obs}}$  of  $8 \pm 1^\circ$ ,  $17 \pm 2^\circ$ , and  $28 \pm 5^\circ$ , respectively, were measured. Figure 4.2(d) presents a plot of the observed magnitude of the pattern rotation from the vertical ( $\theta_{\text{obs}}$ ) as a function of  $\theta_1$ . The trend was well-fit by a line of the form  $\theta_{\text{obs}} = 0.5 \cdot \theta_1 - 1$ . Figure 4.2(e)-(g) presents SEMs representative of photoelectrodeposits that were generated in a manner similar to those presented in Figure 4.2(a). Here,  $\theta_1$  was fixed to a value of  $50^\circ$ , and the ratio of the intensity of this second source to the total intensity,  $[I_1 / (I_0 + I_1)]$ , was adjusted to 0.20 (e), 0.50 (f), and 0.80 (g), respectively. Again, the long axes of the lamellar structures were rotated clockwise away from the vertical in each case, and the magnitude of this rotation ( $\theta_{\text{obs}}$ ) increased with increasing values of the quantity  $I_1 / (I_0 + I_1)$ . For  $I_1 / (I_0 + I_1) = 0.20$ , 0.50, and 0.80, values of  $\theta_{\text{obs}}$  of  $10 \pm 1^\circ$ ,  $23 \pm 5^\circ$ , and  $38 \pm 3^\circ$ , respectively, were observed. Figure 4.2(h) presents a plot of  $\theta_{\text{obs}}$  as a function of the quantity  $I_1 / (I_0 + I_1)$ . The trend was well-fit by a line of the form  $\theta_{\text{obs}} = 0.5 \cdot I_1 / (I_0 + I_1) - 1$ .

Fixed polarization ( $\theta_0 = 0^\circ$ ;  $\theta_1 = 90^\circ$ ), vary intensity

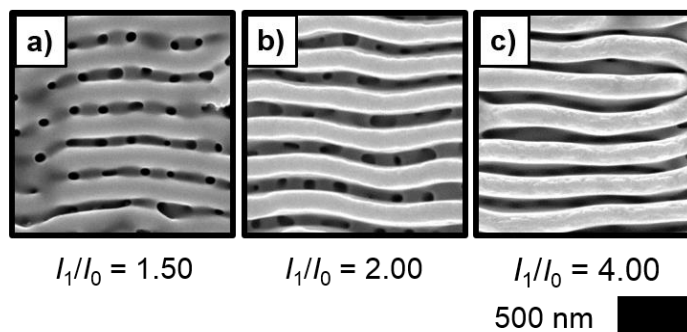


**Figure 4.3.** Photoelectrodeposit morphologies generated using orthogonally polarized same-wavelength sources. (a)-(c) SEMs representative of photoelectrodeposits generated using two  $\lambda_{\text{avg}} = 630$  nm sources, one polarized vertically and the other horizontally, with the indicated intensity ratio between the horizontally and vertically polarized sources ( $I_1/I_0$ ).

Figure 4.3 presents SEMs representative of photoelectrodeposits that were generated using two LED sources with  $\lambda_{\text{avg}} = 630$  nm, with one source polarized vertically with intensity  $I_0$  and the other polarized horizontally with intensity  $I_1$ , wherein  $I_0 \neq I_1$ . The intensity ratio between the horizontally polarized source and the vertically polarized source ( $I_1 / I_0$ ) was 1.50 (a), 2.00 (b), and 4.00 (c). In (a), a square mesh morphology was observed in which a lamellar pattern was produced with the long axes of the lamellae running horizontally, superimposed over another similar pattern in which the long axes of the lamellae ran vertically. The contrast in the SEM suggests that the vertically aligned lamellae were shorter (darker) than those running horizontally. The pattern in (b) is similar to that in (a) but the horizontally oriented lamellae appeared to increase in height relative to the lamellae that ran vertically. In (c) only horizontally running lamellae are visible, and the contrast in the SEM does not suggest the formation of any other structure.

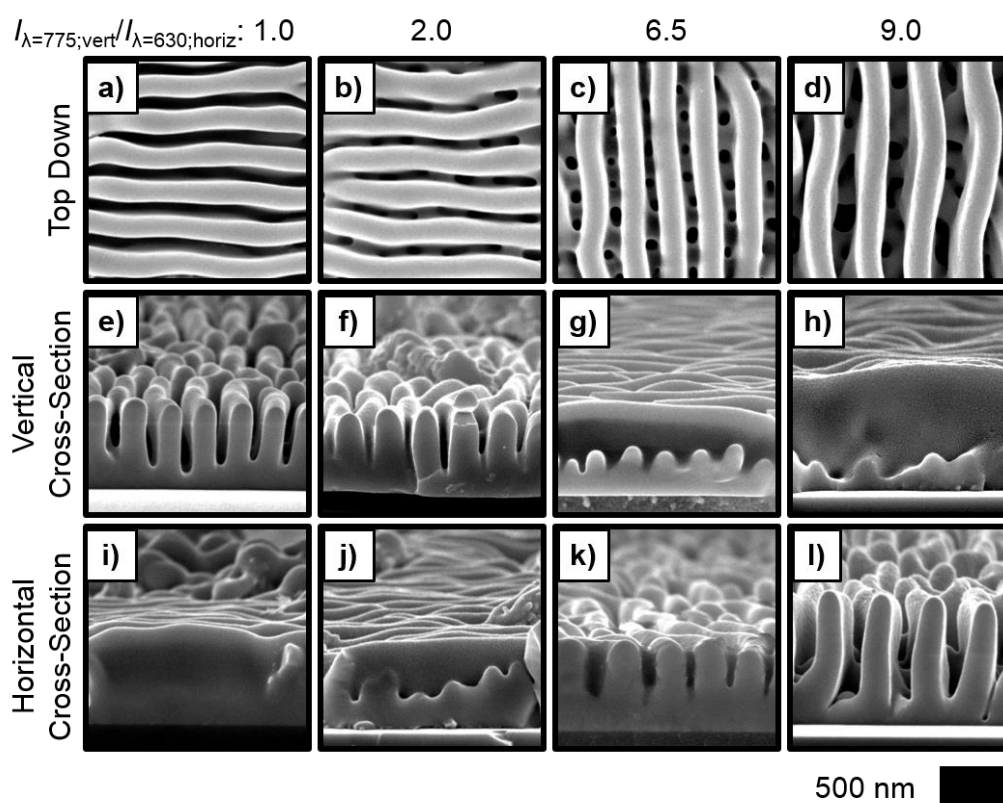
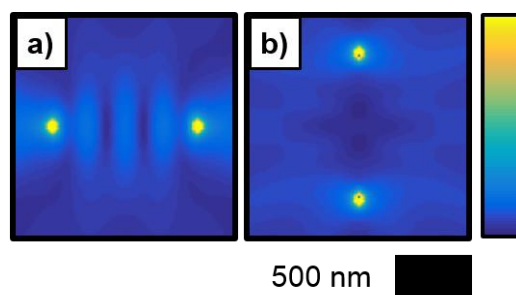


**Figure 4.4.** Photoelectrodeposit morphologies generated using orthogonally polarized sources with differing wavelengths. (a)-(d) Representative SEMs acquired in plan view of photoelectrodeposits generated using simultaneous illumination from a horizontally polarized  $\lambda_{avg} = 630$  nm source and a vertically polarized  $\lambda_{avg} = 775$  nm source with the indicated intensity ratio between the sources ( $I_{\lambda=630;horiz} / I_{\lambda=780;vert}$ ). (e)-(f) Same as (a)-(d) but cleaved along the vertical axis (perpendicular to the polarization of the  $\lambda_{avg} = 630$  nm illumination) and acquired in cross-section. (i)-(l) Same as (a)-(d) but cleaved along the horizontal axis (perpendicular to the polarization of the  $\lambda_{avg} = 775$  nm illumination) and acquired in cross-section.

Figure 4.4(a)-(d) presents a series of top down SEMs that are representative of photoelectrodeposits generated using simultaneous illumination with a LED source with  $\lambda_{avg} = 775$  nm polarized vertically and a LED source with  $\lambda_{avg} = 630$  nm polarized horizontally, with intensity ratios between the two sources ( $I_{\lambda=775;vert} / I_{\lambda=630;horiz}$ ) of 1.0

(a), 2.0 (b), 6.5 (c), and 9.0 (d), respectively. In (a), a lamellar structure was observed in which the long axes of the lamellae were oriented horizontally. The SEM in (b) is similar to that in (a) but displays a small amount of contrast in the spaces between the horizontally running lamellae. In (c), a lamellar structure in which the long axes of the lamellae are oriented vertically is observed. This structure exhibited a larger periodicity than those in (a) and (b). Also, vertically periodic contrast was observed in the space between the lamellae, suggesting the presence of a second set of intersecting lamellae having long axes oriented along the horizontal direction. In (d), like (c), a lamellar structure in which the long axes of the lamellae were oriented vertically was observed, and again the periodicity of this structure was greater than that observed in (a) or (b). Some contrast is visible in the spaces between the vertically running lamellae, but unlike in (c) this contrast did not appear to be periodic. Figure 4.4(e)-(h) and (i)-(l), respectively, present SEMs acquired from the same samples as in (a)-(d), but acquired in cross-sectional view by cleaving the substrate and film along the vertical (perpendicular to the polarization vector of the  $\lambda_{\text{avg}} = 630$  nm illumination during growth), and along the horizontal (perpendicular to the polarization vector of the  $\lambda_{\text{avg}} = 775$  nm illumination during growth), respectively. The cross-sections in (e) and (f) depict horizontally oriented lamellae similar to those seen in (a) and (b) from a perspective looking down the lamellar axes. In (g), a shorter, less well-defined structure similar to those observed in (e) and (f) and with a similar periodicity was observed superimposed on a mostly featureless ridge that is the side of a vertically running lamella similar to those observed in the top down micrograph in (c). In (h), the micrograph reveals a ridge that is also the side of a vertically running lamella, as in (g).

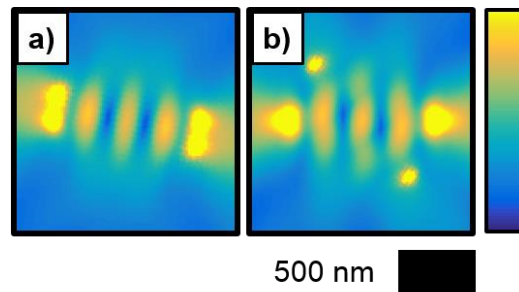
Some superimposed growth is again observed, with a varying height from left to right across the micrograph. In (i), the micrograph reveals a ridge that is the side of a horizontally running lamella similar to those presented in the top down micrograph in (a). In (j), a ridge similar to that observed in (i) is displayed. Superimposed on this ridge is growth with periodically varying height from left to right across the micrograph. The cross-sections in (k) and (l) depict vertically oriented lamellae similar to those seen in (c) and (d), from a perspective looking down the lamellar axes.



**Figure 4.5.** Normalized time-average of electric field magnitude from two dipoles emitting radiation with the same wavelength as a function of separation geometry. Dipoles are emitting radiation with a free space wavelength of  $\lambda = 630$  nm in a medium of index  $n = 1.33$  and are separated by a distance of two wavelengths in the direction (a) perpendicular and (b) parallel to the oscillation axis.

Point dipole radiation sources were used to model the amplitude modulation of the electric field at the active film-solution interface during photoelectrochemical growth that was caused by the inherent surface roughness of the deposited film. The time-averaged field amplitude resulting from two coherent dipole sources was calculated using two-dimensional FDTD simulations. Figure 4.5 presents the normalized time-average of the electric-field magnitude from two dipoles emitting

radiation with a free-space wavelength of  $\lambda = 630$  nm in a medium of index  $n = 1.33$  wherein the dipoles are separated by a distance of two wavelengths. In (a), the dipoles are separated perpendicular to the oscillation axis, and from left to right three strong vertically running interference fringes were observed in the area between the dipoles. In (b), the dipoles are separated parallel to the oscillation axis, and constructive interference between the dipoles was not observed.



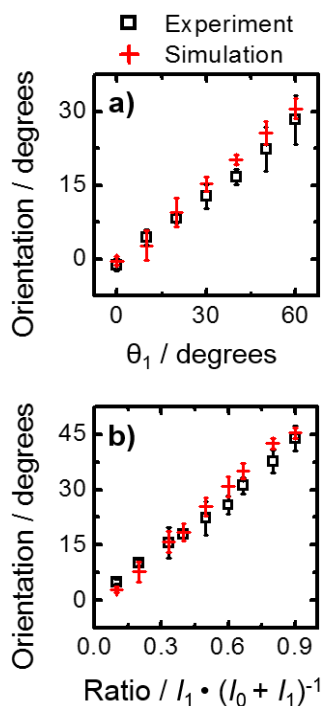
**Figure 4.6.** Normalized time-average of electric field magnitude resulting from two incoherently summed sets of dipole pairs each aligned perpendicular to a direction of oscillation. Dipoles are emitting radiation with a free space wavelength of  $\lambda = 630$  nm in a medium of index  $n = 1.33$ . (a) One dipole set separated by two wavelengths along the horizontal axis and the axis of separation of the other set is rotated  $\theta = 20^\circ$  clockwise from the horizontal, and both sets emit radiation with equal intensity. (b) One dipole set separated by two wavelengths along the horizontal axis and the axis of separation of the other set is rotated by  $\theta = 50^\circ$  clockwise from the horizontal, and the two sets emit radiation with relative intensity  $I_{\text{rotated}} / (I_{\text{rotated}} + I_{\text{horizontal}}) = 0.2$ .

Figure 4.6 presents simulations similar to those in Figure 4.5 but with two incoherently summed sets of coherent dipole pairs aligned perpendicular to a direction of oscillation. In (a), one dipole set is separated along the horizontal axis while the axis of separation of the other is rotated  $\theta = 20^\circ$  clockwise from the horizontal, and both

sets emit radiation with equal intensity. Interference fringes similar to those displayed in Figure 4.5(a) were observed but were rotated clockwise from the vertical by  $\theta_{\text{obs}} = 10^\circ$ . In (b), one dipole set is separated along the horizontal axis while the axis of separation of the other is rotated  $\theta = 50^\circ$  clockwise from the horizontal, and the two sets were simulated to emit radiation with a relative intensity  $I_{\text{rotated}} / (I_{\text{rotated}} + I_{\text{horizontal}}) = 0.2$ . Interference fringes similar to those in (a) were observed, and the most intense parts of the fringes were measured to be rotated clockwise from the vertical by  $\theta_{\text{obs}} = 9^\circ$ .

Computer modeling of the photoelectrochemical growth process was performed to analyze the morphologies expected for films generated as a result of the fundamental light-matter interactions during the deposition, using simultaneous illumination with two same-wavelength sources having different linear polarizations. The two-step, iterative model described in Chapter 1 was utilized wherein electromagnetic simulations were first used to calculate the local photocarrier-generation rates at the electrode/solution interface and then electrochemical addition of mass was simulated via a Monte Carlo method that utilized the local photocarrier-generation rate to weight the local probabilities of mass. During the early stages of deposition, dipole sources could be used to represent point-like scattering features due to surface roughness of the deposit and help to visualize the periodic absorption profile that occurs between two scattering features along the growth front. However, at later times, these interfacial features evolved into anisotropic structures that had an extended spatial structure. Utilization of the modeling algorithm, which recalculated the scattering and absorption profile as the film morphology evolved, enabled the

growth process to be fully reproduced. The model both incorporated the absorption modulation resulting from surface roughness during the early stages of growth and also captured the dynamic feedback between light absorption and material growth which resulted in 3D structures that agreed with experiment.



**Figure 4.7.** Orientation of photoelectrodeposit morphologies generated using two same-wavelength sources with differing linear polarization derived computationally from growth modeling compared to experimental results. (a) Plot of the orientation of the pattern long-axis ( $\theta_{\text{obs}}$ ) measured clockwise from the vertical as a function of the polarization orientation of one source ( $\theta_1$ ) for two-source illuminated photoelectrodepositions with same-wavelength ( $\lambda_{\text{avg}} = 630$  nm), equal intensity sources when the other source was polarized vertically ( $\theta_0 = 0^\circ$ ). (b) Plot of  $\theta_{\text{obs}}$  as a function of the fraction of the total intensity [ $I_1 / (I_0 + I_1)$ ] delivered by a source polarized linearly  $\theta_1 = 50^\circ$  clockwise from the vertical in two-source illuminated photoelectrodepositions with same-wavelength sources when the other source was polarized vertically.

The experiment described in Figure 4.2(a)-(d) was simulated, wherein two equal intensity sources with  $\lambda_{\text{avg}} = 630$  nm were utilized and one source was polarized vertically while the polarization of the second source was offset clockwise from the vertical by  $\theta_1$ , and the observed rotation of the long-axis of the lamellar pattern clockwise away from the vertical ( $\theta_{\text{obs}}$ ) was derived. Figure 4.7(a) presents a plot of both the experimentally and computationally derived values of  $\theta_{\text{obs}}$  as a function of  $\theta_1$ . The experiment described in Figure 4.2(e)-(h) was also simulated, wherein the two sources with  $\lambda_{\text{avg}} = 630$  nm were again utilized, with one source polarized vertically and the other at  $\theta_1 = 50^\circ$  from the vertical in the clockwise direction, while the fraction of the total intensity delivered by the second source  $[I_1 / (I_0 + I_1)]$  was varied. Figure 4.7(b) presents a plot of both the experimentally and computationally derived values of  $\theta_{\text{obs}}$  for this experiment as a function of  $[I_1 / (I_0 + I_1)]$ . For both experiments, the empirically and computationally derived values of  $\theta_{\text{obs}}$  were in good agreement, and were linear functions of either  $\theta_1$  or  $[I_1 / (I_0 + I_1)]$ .

Fixed polarization ( $\theta_0 = 0^\circ$ ;  $\theta_1 = 90^\circ$ ), vary intensity

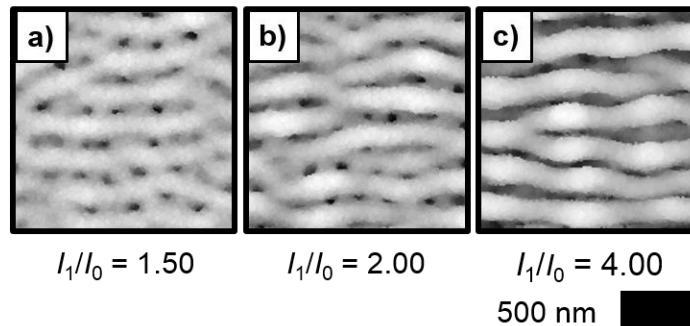


**Figure 4.8.** Simulated photoelectrodeposit morphologies generated using orthogonally polarized same-wavelength sources. (a)-(c) Simulated morphologies generated using two  $\lambda_{\text{avg}} = 630$  nm sources, the first polarized vertically and the second horizontally, with the indicated intensity ratio between the horizontally and vertically polarized sources ( $I_1/I_0$ ).

Additionally, computer modeling of the growth process was also performed to simulate the morphologies expected for films generated using simultaneous illumination from two orthogonally polarized, same-wavelength sources with unequal intensities. The experiment described in Figure 4.3(a)-(c) was modeled (Figure 4.8), wherein two unequal intensity sources with  $\lambda_{\text{avg}} = 630$  nm were utilized with one source polarized vertically and the other horizontally. The intensity ratio between the horizontally polarized source and the vertically polarized source ( $I_1 / I_0$ ) was 1.50 (a), 2.00 (b), and 4.00 (c), respectively. The simulated morphologies were in close accord with those observed experimentally (Figure 4.3), producing a square mesh morphology wherein the horizontally oriented lamellae were taller than those oriented vertically for  $I_1 / I_0 = 1.50$  and 2.00, and producing a single, horizontally oriented lamellar morphology for  $I_1 / I_0 = 4.00$ .

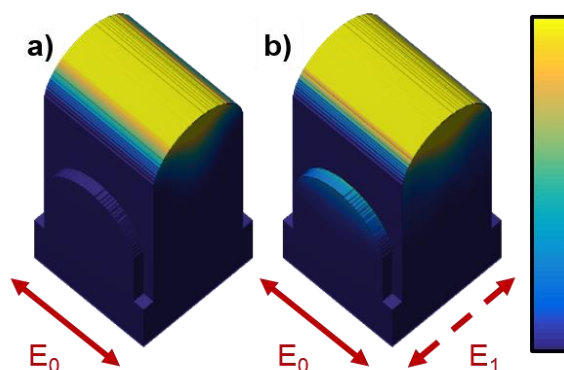


**Figure 4.9.** Computational analysis of light absorption in idealized models of structures generated via photoelectrodeposition using orthogonally polarized same-wavelength sources. (a) Simulated power absorption of two idealized, orthogonal lamellae under  $\lambda = 630$  nm plane wave illumination polarized parallel to the taller feature ( $E_0$ ). The width of each structure is typical of lamellar structures generated via photoelectrodeposition with  $\lambda_{\text{avg}} = 630$  nm illumination and the length of each lamella is typical of one period of such structures. (b) Same as (a) but with the addition of a second  $\lambda = 630$  nm source with 0.5 times the intensity of the first and polarized perpendicular to the taller feature ( $E_1$ ) (sources assumed to be incoherent).

To further understand the growth of the morphologies that were observed when two orthogonally polarized sources of differing intensities and/or wavelengths were utilized, three sets of simulations of light absorption in idealized intersecting lamellar features were performed. First, films that had been experimentally photoelectrodeposited under vertically polarized  $\lambda_{\text{avg}} = 630$  nm illumination alone and 775 nm illumination alone were analyzed using SEM to derive the lamellar periods and widths of the resultant structures. These values were then used as the inputs for the lengths and widths of the idealized structures. Two idealized lamellae were oriented so as to intersect at a  $90^\circ$  angle and were assigned heights of 200 nm and 400 nm. In the first set of simulations, designed to help understand the growth of the morphologies

that were observed when two orthogonally polarized sources with the same wavelength were used ( $\lambda_{\text{avg}} = 630$  nm; Figure 4.3), the two lamellae both had widths that corresponded to the width of the lamellar structures observed for deposition with  $\lambda_{\text{avg}} = 630$  nm illumination alone, and both had lengths equal to the corresponding lamellar period. Figure 4.9 presents the power absorption profile calculated (a) from a single  $\lambda = 630$  nm plane wave source polarized parallel to the long axis of the taller lamella and (b) from two  $\lambda = 630$  nm plane wave sources wherein one source was polarized parallel and the other perpendicular to the long axis of the taller lamella, with the source polarized perpendicular having half the intensity of the one polarized parallel. Figure 4.9(a) shows that significant absorption was observed only near the tip of the taller lamella. Figure 4.9(b) indicates that absorption was observed both at the tip of the taller lamella as well as at the tip of the shorter lamella.

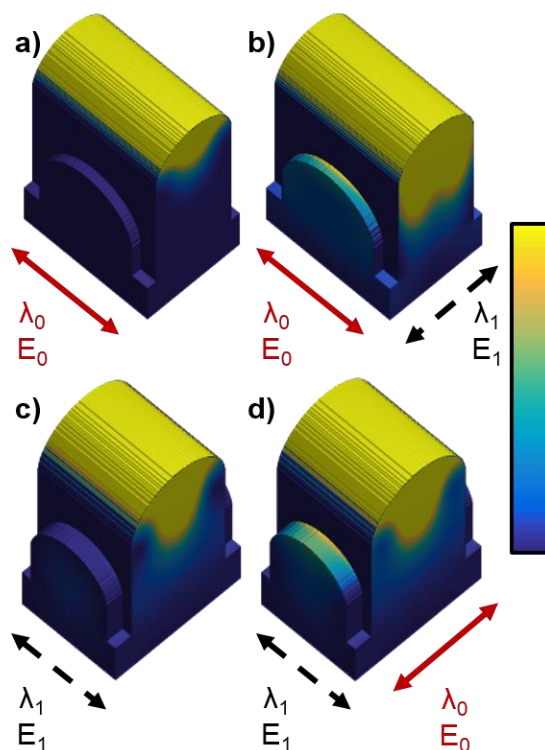


**Figure 4.10.** Computational analysis of light absorption in idealized models of structures generated via photoelectrodeposition using orthogonally polarized sources with differing wavelengths. (a) Simulated power absorption of two ideal orthogonal lamellae under  $\lambda_0 = 630$  nm plane wave illumination polarized parallel to the taller feature ( $E_0$ ). The width of the taller structure is typical of lamellar structures generated via photoelectrodeposition with  $\lambda_{\text{avg}} = 630$  nm illumination whereas the width of the shorter structure is typical of the structures generated with  $\lambda_{\text{avg}} = 775$  nm illumination. (b) Same as (a) but with the addition of a  $\lambda_1 = 775$  nm plane wave source with twice the intensity of the  $\lambda_0 = 630$  nm source and polarized perpendicular to the taller feature ( $E_1$ ) (sources assumed to be incoherent). (c) Simulated power absorption of two ideal orthogonal lamellae under a  $\lambda_1 = 775$  nm plane wave source polarized parallel to the taller feature ( $E_1$ ). The width of the taller structure is typical of lamellar structures generated via photoelectrodeposition with  $\lambda_{\text{avg}} = 775$  nm illumination whereas the width of the shorter structure is typical of the structures generated with  $\lambda_{\text{avg}} = 630$  nm illumination. (d) Same as (c) but with the addition of a  $\lambda_0 = 630$  nm plane wave source 6.5 times less intense than the 775 nm source and polarized perpendicular to the taller feature ( $E_0$ ) (sources assumed to be incoherent).

The second and third sets of light absorption simulations were designed to help understand the generation of the morphologies observed when two orthogonally polarized sources with  $\lambda_{\text{avg}} = 630$  nm and  $\lambda_{\text{avg}} = 775$  nm were utilized simultaneously (Figure 4.4). In the second set of simulations, the taller lamellar feature had a width corresponding to the width of the lamellar structures observed for deposition with  $\lambda_{\text{avg}} = 630$  nm illumination alone, and the length of the shorter lamella was equal to the corresponding lamellar period. The shorter lamellar feature had a width corresponding to the width of the lamellar structures observed for deposition with  $\lambda_{\text{avg}} = 775$  nm illumination alone, and the length of the taller lamella was equal to the corresponding lamellar period. Figure 4.10(a) and (b), respectively, present the power absorption profile calculated from a single  $\lambda = 630$  nm plane-wave source polarized parallel to the long axis of the taller lamella alone, and from the same source as in (a) as well as a secondary  $\lambda = 775$  nm plane-wave source polarized perpendicular to the long axis of the taller lamella that was twice as intense as the  $\lambda = 630$  nm source. In Figure 4.10(a), significant absorption was observed only near the tip of the taller lamella. In Figure 4.10(b), absorption was observed both at the tip of the taller lamella as well as at the tip of the shorter lamella. The third set of simulations utilized lamellar structures having similar dimensions as the second set but with the heights of the two lamellae exchanged. Figure 4.10(c) and (d), respectively, present the power absorption profile calculated from a single  $\lambda = 775$  nm plane-wave source polarized parallel to the long axis of the taller lamella alone, and from the same source as in (c) as well as a secondary  $\lambda = 630$  nm plane wave source polarized perpendicular to the long axis of the taller lamella that was 6.5 times less intense than the  $\lambda = 775$  nm source. As with

the second set of simulations (Figure 4.10(a)-(b)) in Figure 4.10(c) significant absorption was observed only near the tip of the taller lamella, whereas in Figure 4.10(d) absorption was observed both at the tip of the taller lamella as well as at the tip of the shorter lamella.

When two sources having the same wavelength ( $\lambda_{\text{avg}} = 630 \text{ nm}$ ) but having differing, linear, non-orthogonal polarizations were utilized simultaneously (Figure 4.2(a)-(c) and (e)-(g)), a lamellar pattern identical to those observed with only a single source (Figure 4.1) was observed, except for an in-plane rotation. This result can be readily understood because any linear polarization can be equivalently expressed as the sum of two orthogonal linear polarizations, e.g. vertical and horizontal. Thus, no difference may be observed between the morphology generated if a single illumination source is utilized relative to the morphology generated if two sources are used simultaneously, as long as the intensity-weighted average of the polarization orientations of the two tandem sources is the same as the polarization of the single source. The experimental data quantitatively supports this hypothesis, because the observed orientation of the pattern ( $\theta_{\text{obs}}$ ) for the two-source experiments was almost exactly equal to the intensity-weighted average polarization orientation:  $(I_0 \cdot \theta_0 + I_1 \cdot \theta_1) / (I_0 + I_1)$ . For the experiment wherein the intensity of the sources was equal ( $I_0 = I_1$ ), the first source was polarized vertically ( $\theta_0 = 0^\circ$ ) and the angle between the polarization vectors ( $\theta_1$ ) was varied,  $\theta_{\text{obs}}$  would be expected to have the form  $0.5 \cdot \theta_1$ . This expectation is very close to the experimentally observed relation of  $\theta_{\text{obs}} = 0.5 \cdot \theta_1 - 1$ . Similarly, for the experiment in which the polarizations of the two sources were fixed ( $\theta_0 = 0^\circ$  and  $\theta_1 = 50^\circ$ ) and the relative contribution of the two sources to the

total intensity was varied,  $\theta_{\text{obs}}$  would be expected to have the form  $50 \cdot [I_1 / (I_0 + I_1)]$ , which again is very close to the experimentally observed relation of  $\theta_{\text{obs}} = 50 \cdot [I_1 / (I_0 + I_1)] - 1$ . The difference between the expected and experimentally observed relations for  $\theta_{\text{obs}}$ , a  $-1^\circ$  offset, is likely a minor systematic error arising from a minor calibration error in a polarizer setting. This notion is supported by the facts that a value of  $\theta_{\text{obs}} = -1 \pm 1^\circ$  was observed when  $\theta_0 = \theta_1 = 0^\circ$ , and that the experimentally observed values of  $\theta_{\text{obs}}$  were generally marginally lower than expected.

The quantitative agreement between the values of  $\theta_{\text{obs}}$  measured in the experiments using same-wavelength ( $\lambda_{\text{avg}} = 630 \text{ nm}$ ) sources with mutually different linear, non-orthogonal polarizations simultaneously, and in the analogous computer simulations (Figure 4.7), which utilized minimal empirical data, for all investigated conditions, suggests that the empirically observed behavior is the result of a fundamental optical phenomenon. This notion is supported by the results of the dipole scattering simulations (Figure 4.5 and 4.6). The interference fringes observed between two simulated radiation-emitting dipoles separated along the horizontal axis, and perpendicular to the oscillation axis, (Figure 4.5(a)) are reminiscent of the lamellar morphology observed in the photoelectrodeposit generated with vertically polarized illumination (Figure 4.1(a)), and have been hypothesized to promote the initial growth of this periodic and anisotropic structure by providing the necessary spatially varying distribution of light intensity.<sup>47</sup> When two sets of dipoles were simulated with some angle,  $\theta$ , between their axes of separation, the resultant interference fringes were observed to rotate by an angle,  $\theta_{\text{obs}}$ , that is in good agreement with relation of  $\theta_{\text{obs}} = \theta \cdot [I_{\text{rotated}} / (I_{\text{rotated}} + I_{\text{horizontal}})]$ . Thus, the dipole scattering simulations suggest that the

orientation of the lamellar structures in the non-orthogonal, same-wavelength experiments is a manifestation of the elementary phenomenon of superposition of waves.

When two orthogonally polarized same-wavelength ( $\lambda_{\text{avg}} = 630 \text{ nm}$ ) sources that had unequal mutual intensities were utilized, the resultant structures appeared to consist of two intersecting sets of orthogonally oriented lamellae wherein the relative heights of each set of lamellae were directly proportional to the relative source intensities (Figure 4.3). These observations indicate that the utilization of orthogonally polarized sources can enable independent control over different features of the resultant film morphology, and thus comprises a potentially useful tool for generating application-specific structures. The reproduction of the experimental morphologies by the growth model (Figure 4.8) suggests that the generation of the intersecting structures when orthogonally polarized light is used is a result of the intrinsic light-matter interactions that occur during the deposition process. Moreover, the continued growth of such intersecting structures under the aforementioned conditions is consistent with the simulations of light absorption in the idealized versions of the structures (Figure 4.9) wherein illumination from two orthogonally polarized sources is preferentially absorbed in the tips of both structures. These areas represent the photoelectrochemical growth fronts: preferential light absorption in these areas supports continued anisotropic growth in a manner that preserves the cross sections of the features. Furthermore, visualization of the difference in the absorption profile with and without the contribution from the source parallel to the shorter feature

indicated that this source was solely responsible for absorption along the shorter feature.

Intersecting lamellar structures were also observed when two orthogonally polarized sources with differing wavelengths ( $\lambda_{\text{avg}} = 630 \text{ nm}$  and  $775 \text{ nm}$ ) were utilized. Again, the relative heights of each set of lamellae were proportional to the relative source intensities. However, for  $I_{\lambda=775;\text{vert}} / I_{\lambda=630;\text{horiz}} = 1.0$ , SEM analysis provided little evidence for the presence of periodic, anisotropic structures with long axes oriented along the vertical, and, for  $I_{\lambda=775;\text{vert}} / I_{\lambda=630;\text{horiz}} = 2.0$ , such structures were found to be shorter than the simultaneously observed, horizontally-oriented structures. Also, for  $I_{\lambda=775;\text{vert}} / I_{\lambda=630;\text{horiz}} = 6.5$  and  $9.0$ , structures with horizontal periodicity were observed. These observations are consistent with previous physical characterization suggesting that lower rates of photoelectrodeposition may be observed when utilizing  $\lambda = 775 \text{ nm}$  than when utilizing  $\lambda = 630 \text{ nm}$  illumination.

Unlike the intersecting lamellar structures generated using two orthogonally polarized same-wavelength sources ( $\lambda_{\text{avg}} = 630 \text{ nm}$ ), when two orthogonally polarized sources with differing wavelengths ( $\lambda_{\text{avg}} = 630 \text{ nm}$  and  $775 \text{ nm}$ ) were used, the periodicities of two sets of lamellae were unequal. The set with their long axes oriented parallel to the polarization vector of the  $\lambda_{\text{avg}} = 775 \text{ nm}$  source displayed a greater periodicity than those oriented parallel to the polarization vector of the  $\lambda_{\text{avg}} = 630 \text{ nm}$  source. This difference in periodicity is a consequence of differing anisotropic light absorption profiles in the growing structures in response to the different wavelengths, and the lamellar period increases monotonically with  $\lambda$ .<sup>47</sup> Moreover, these results indicate that not only is it possible to control the relative heights of structures with

orthogonal periodicities, but also indicate that the magnitudes of those periodicities can also be controlled, which may be of use in the construction of purpose-designed structures. Simulations in idealized versions of these intersecting structures were again consistent with their growth (Figure 4.10): illumination polarized along the long axis of a lamellar structure (of the same wavelength used to generate that structure) is preferentially absorbed in the tip of that structure relative to light polarized perpendicularly (of a different wavelength).

Dynamic photoelectrochemical growth may find potential in the generation of nanophotonic optical elements including planar lenses and mirrors,<sup>69-71</sup> polarization-sensitive filters and photodetectors,<sup>72</sup> and nanostructured scaffolds.<sup>73,74</sup> The results described in this chapter have several implications for the use of this process to design application-targeted structures. First, controlling the pattern orientation with respect to the substrate does not require changing the polarization state of a single source, for example, rotating a linear polarizer. Instead, two sources could be used with static linear polarizations and the pattern orientation could be controlled by changing the relative intensity of the sources. Manipulating such a quantity continuously or in discrete steps over time could be used to generate morphological complexity. The utilization of orthogonal sources also presents another method to generate intricate structures wherein control of the feature size in three dimensions of two patterns may be obtained simultaneously and independently.

### 4.3 Conclusions

Nanopatterned Se-Te films were photoelectrochemically prepared using simultaneous illumination from two light sources with discrete linear polarizations. Films grown with two non-orthogonally polarized, same-wavelength sources displayed lamellar morphologies wherein the long axes of the structures were aligned along the intensity-weighted average polarization vector. Such behavior was consistent with simulations of light scattering at the solution-film interface at the onset of photoelectrochemical growth. Simulations of the growth with such illumination showed that the emergence of the observed morphologies could be understood by considering the fundamental light-matter interactions during deposition. Structures consisting of two sets of intersecting, orthogonal lamellae were generated when two orthogonally polarized illumination sources were utilized wherein the periodicity and feature size of each set of lamellae was proportional to the wavelengths of the illumination source polarized along their long axes. The evolution of such morphologies was consistent with simulations of light absorption in idealized intersecting lamellar structures, which indicated that the lamellae preferentially absorbed light polarized along with the electric field vector parallel to the long axes. The cumulative data suggest that under the conditions investigated, the morphology of the photoelectrodeposit is sensitive simultaneously to the polarization of both sources utilized during growth. Additionally, the use of such tailored optical excitation provides control over the pattern orientation and enables the generation of three-dimensional structures that cannot be produced with a single polarization.

*Chapter 5***MORPHOLOGICAL EXPRESSION OF THE COHERENCE AND  
RELATIVE PHASE OF OPTICAL INPUTS TO THE  
PHOTOELECTRODEPOSITION OF NANOPATTERNED SE-TE  
FILMS**

Carim, A. I.; Batara, N. A.; Premkumar A.; May, R.; Atwater, H. A.; Lewis, N. S. *Nano Letters*, **2016**, *16*, 2963-2968. DOI: 10.1021/acs.nanolett.5b04999

**5.1 Introduction**

In this chapter, the morphologies of Se-Te photoelectrodeposits generated using two same-wavelength illumination sources were investigated with a series of discrete linear polarizations in tandem, either both mutually incoherent or mutually coherent with defined phase differences. In conjunction with the experiments, the morphologies of the resulting deposits were simulated by computational modeling of the light-material interactions intrinsic to the photoelectrochemical growth process. This collective assessment examines the capacity of the deposition process to generate unique morphologies in response to discrete net polarization states, and thus to display sensitivity toward the coherency, phase difference, and polarization orientations of the optical inputs. Such further elaboration of the relationship between the illumination and resultant morphology enables the use of deliberately tailored excitation to tune the programmable growth of the deposited material.

## 5.2 Results and Discussion

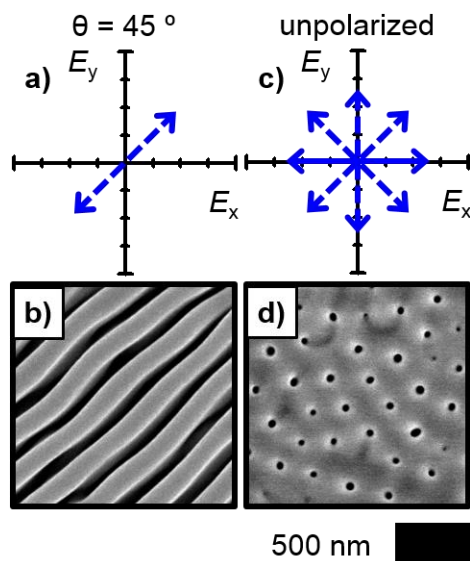


**Figure 5.1.** Effect of illumination source polarization on anisotropy and orientation of photoelectrodeposit morphology. (a) Plot of the E-field vector of a LED source with  $\lambda_{\text{avg}} = 630$  nm linearly polarized  $45^\circ$  clockwise from the vertical, and (b) SEM representative of a photoelectrodeposit generated with this source. (c) Plot illustrative of the many E-field vectors characteristic of the same source as in (a) when unpolarized, and (d) SEM representative of a photoelectrodeposit generated with such source in the unpolarized state.

Se-Te photoelectrodeposits were generated using illumination from a single LED source with  $\lambda_{\text{avg}} = 630$  nm and which was linearly polarized such that the E-field component was oriented at an angle  $\theta = 45^\circ$  clockwise from the vertical as indicated in the plot presented in Figure 5.1(a). Figure 5.1(b) presents a representative SEM of the deposit morphology which reveals a highly anisotropic lamellar-type morphology wherein the long axes of the lamellae are oriented parallel to the direction of the E-field during growth.<sup>47,58,59</sup> Quantitatively, the long axes of the lamellae were oriented at  $45 \pm 3^\circ$  clockwise from the vertical ( $\theta_{\text{obs}}$ ). Deposits were also generated in the same

manner as in (b), but without the use of any polarizing optic, so that the illumination was unpolarized as indicated in the plot presented in Figure 5.1(c), and a representative SEM is presented in Figure 5.1(d). The use of unpolarized light resulted in the generation of an ordered, isotropic mesh-type morphology that consisted of an array of nanopores. Thus, both linearly polarized and unpolarized illumination effect material patterning, but the asymmetry inherent in the linearly polarized illumination creates morphological anisotropy and directs the orientation of the lamellae in the photoelectrodeposit.

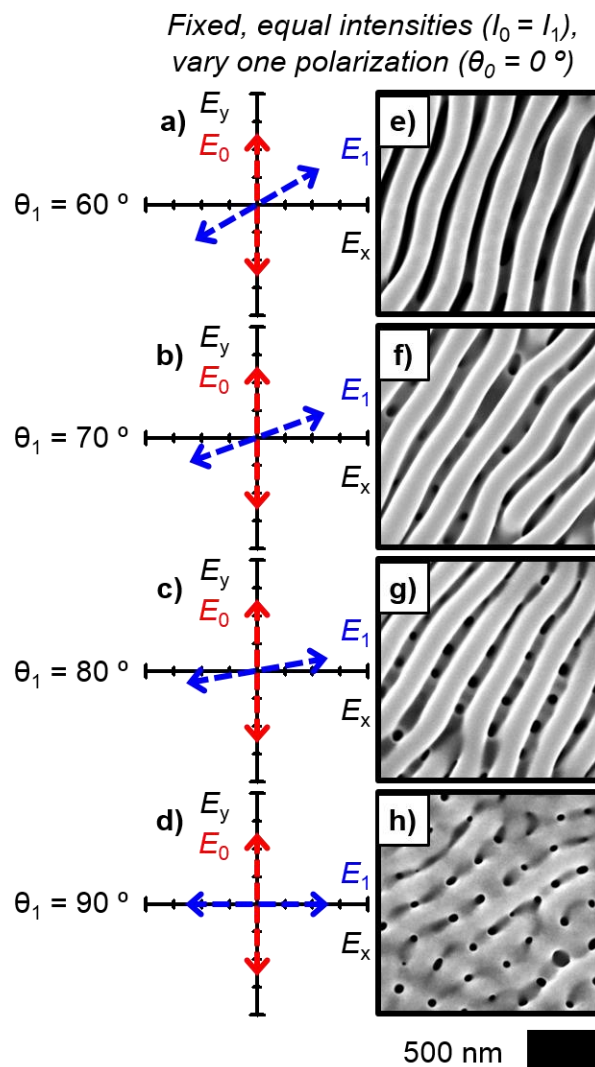


**Figure 5.2.** Two-source illumination polarization effect on photoelectrodeposit morphology for near-orthogonal and orthogonal polarizations. (a)-(d) Plots of the E-field vectors,  $E_0$  and  $E_1$ , of two incoherent LED sources with  $\lambda_{\text{avg}} = 630$  nm and equal intensity, the first source polarized vertically ( $\theta_0 = 0^\circ$ ) and the second at the indicated rotation ( $\theta_1$ ) clockwise from the vertical, and (e)-(h) SEMs representative of photoelectrodeposits generated using these sources.

Subsequent deposits were generated by simultaneously using two incoherent LED sources that had  $\lambda_{\text{avg}} = 630$  nm and equal intensities, with the first source polarized vertically ( $\theta_0 = 0^\circ$ ) and the second source offset clockwise from the vertical

by  $\theta_1 = 60^\circ, 70^\circ, 80^\circ,$  or  $90^\circ$ . The E-field vectors of each of the two tandem sources are plotted for each condition in Figure 5.2(a)-(d). SEMs representative of the resultant deposit morphologies are presented in Figure 5.2(e)-(h). With  $\theta_1 = 60^\circ$ , a lamellar-type morphology, similar to that generated with a single illumination source, was observed (Figure 5.2(e)), with a value of  $\theta_{\text{obs}} = 27 \pm 4^\circ$ . This value agrees with the intensity-weighted average polarization orientation,  $0.5 \cdot \theta_1$  for the conditions here, or specifically  $30^\circ$  for the case of  $\theta_1 = 60^\circ$ , and is consistent with behavior observed previously for  $0^\circ < \theta_1 < 60^\circ$ .<sup>59</sup> Such agreement suggests that essentially identical morphologies should be generated using either a single linearly polarized source with orientation  $\theta$ , or two linearly polarized sources having an average polarization orientation  $\theta$ . However, when the difference between the polarization orientations of the sources increased past  $\theta_1 \approx 60^\circ$ , the morphologies observed for the use of two same-wavelength (630 nm) sources with equal intensities, but differing linear polarizations, were more complex than simple lamellar patterns (Figure 5.2(f)-(h)). Beyond this limit, oriented lamellae were still observed, and, for  $\theta_1 = 70^\circ, 80^\circ,$  and  $90^\circ$ ,  $\theta_{\text{obs}} = 32 \pm 6^\circ, 38 \pm 5^\circ,$  and  $46 \pm 8^\circ$ , respectively. The behavior is thus consistent with expectations based on the average polarization orientation. However, as  $\theta_1$  was increased, a mesh-type pattern at a height lower than the diagonal-running lamellae also became apparent (Figure 5.2(f)-(h)), and when  $\theta_1 = 90^\circ$  (Figure 5.2(h)) the height of this pattern approached the height of the lamellae. The morphology observed when  $\theta_1 = 90^\circ$  (Figure 5.2(h)) was not identical to that generated with a single source oriented at  $\theta = 45^\circ$  (Figure 5.1(b)), but rather exhibited significantly less-defined

anisotropy, resembling an average of the morphologies observed for the single source oriented at  $\theta = 45^\circ$  and for the unpolarized source (Figure 5.1(d)).

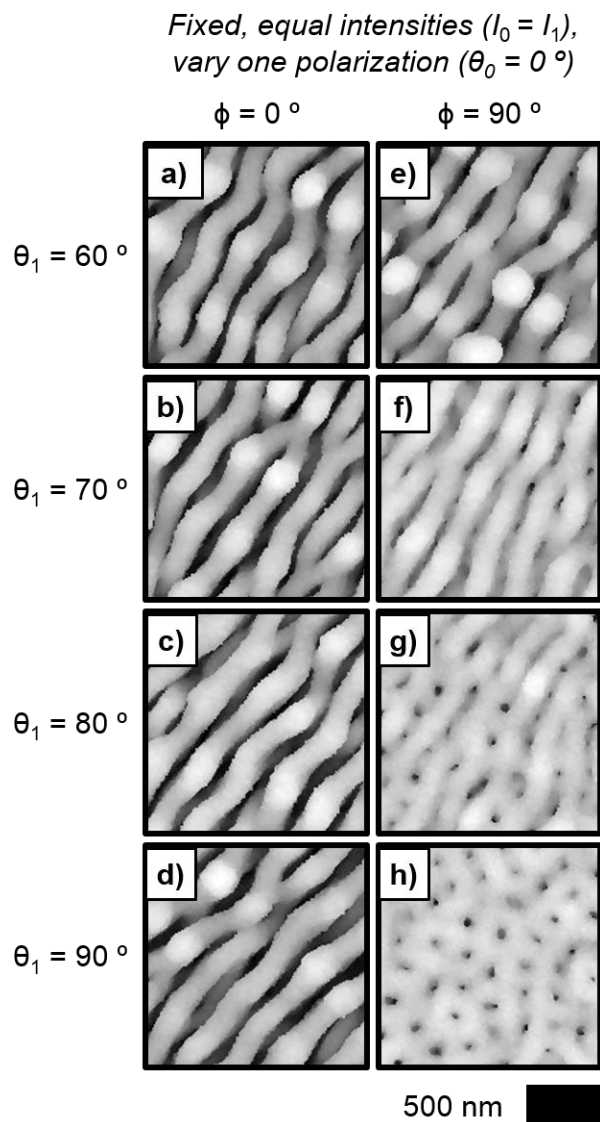


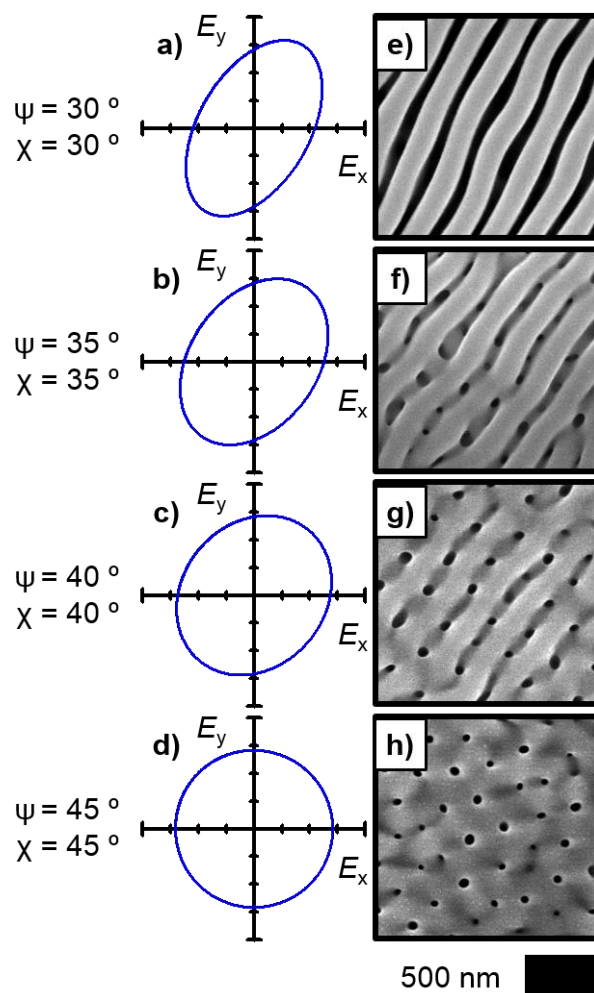
**Figure 5.1.** Simulated photoelectrodeposit morphologies generated using two fully in-phase or fully out-of-phase coherent, same-wavelength sources with equal intensities and near-orthogonal or orthogonal polarizations.  $\lambda = 630$  nm for both sources. The first source is polarized vertically ( $\theta_0 = 0^\circ$ ) and the second at the indicated rotation ( $\theta_1$ ) clockwise from the vertical. Simulations are presented under two conditions: one with a phase angle between the two coherent sources of  $\phi = 0^\circ$  (fully in-phase) (a)-(d), and with  $\phi = 90^\circ$  (fully out-of-phase) (e)-(h). In both (a)-(d) and (e)-(h) the E-field vectors of the two sources are as indicated in Figure 2(a)-(d), respectively.

The appearance of the mesh-like component of the morphology, and the associated reduction of the uniaxial anisotropy, is consistent with the incoherent nature of the illumination sources utilized in these experiments. Computer modeling of the photoelectrochemical growth process was consequently performed to simulate the morphologies expected for films generated using simultaneous illumination with two coherent sources. The two-step, iterative model described in Chapter 1 was utilized wherein electromagnetic simulations were first used to calculate the local photocarrier-generation rates at the electrode/solution interface and then electrochemical addition of mass was simulated via a Monte Carlo method that utilized the local photocarrier-generation rate to weight the local probabilities of mass. Thus, the computational results were principally defined by the fundamental light-matter interactions during deposition. Simulations similar to the experiments described in Figure 5.2 were performed, wherein two equal-intensity sources with  $\lambda_{\text{avg}} = 630$  nm were utilized, with one source polarized vertically and the polarization of the second source offset clockwise from the vertical by  $\theta_1$ . However, unlike the experiment wherein incoherent sources were utilized, the simulations considered coherent sources. Simulations were performed for phase angles ( $\phi$ ) of either  $0^\circ$  or  $90^\circ$  between the two coherent sources. Figure 5.3(a)-(d) present simulations for  $\theta_1 = 60^\circ, 70^\circ, 80^\circ,$  and  $90^\circ$ , respectively, for  $\phi = 0^\circ$ . The E-field vectors of the considered sources were identical to those plotted in Figure 5.2(a)-(d). In each case, a lamellar pattern was observed, and the orientation of the lamellar long axes displayed increasing rotations from the vertical with increasing values of  $\theta_1$ . Specifically, values of  $\theta_{\text{obs}}$  of  $33 \pm 3^\circ, 36 \pm 2^\circ, 40 \pm 2^\circ,$  and  $45 \pm 1^\circ$  were measured for  $\theta_1 = 60^\circ, 70^\circ, 80^\circ,$  and  $90^\circ$ , respectively. Figure 5.3(e) and (f)

present simulations analogous to those shown in Figure 5.3(a)-(d), but for a phase angle of  $\phi = 90^\circ$ . The E-field vectors of the sources were again identical to those presented in Figure 5.2(a)-(d). For  $\theta_1 = 60^\circ$  (Figure 5.3(e)), the simulated morphology was lamellar and qualitatively similar to that observed with  $\phi = 0^\circ$  (Figure 5.3(a)), whereas for  $\theta_1 = 70^\circ$  (Figure 5.3(f)), the simulated morphology also displayed an oriented, lamellar-type component but appeared to be superimposed upon a mesh-type pattern. When  $\theta_1 = 80^\circ$  (Figure 5.3(g)), the lamellar pattern was less well-defined and more similar in height to the mesh-type pattern, relative to the case of  $\theta_1 = 70^\circ$ . Moreover, when  $\theta_1 = 90^\circ$  (Figure 5.3(h)), the morphology lacked any apparent anisotropy and orientation, and was thus similar to the morphology observed experimentally for growth stimulated by a single, unpolarized, incoherent source (Figure 5.1(d)).

The simulated morphologies displayed in Figure 5.3(a)-(d) showed that in the case of coherent sources with a phase difference of  $\phi = 0^\circ$ , only lamellar morphologies were observed. The sum of the output of two completely in-phase, coherent, linearly-polarized, same-wavelength sources cannot be differentiated from the output of a single coherent, linearly-polarized source that has an equivalent net intensity and the same polarization orientation as the weighted average polarization orientation of the tandem sources. Consequently, the photoelectrodeposit morphology observed for the case of a single incoherent source polarized at  $\theta = 45^\circ$  (Figure 5.1(b)) was qualitatively matched by the simulated morphology for two equal intensity, in-phase ( $\phi = 0^\circ$ ) coherent sources polarized at  $\theta_0 = 0^\circ$  and  $\theta_1 = 90^\circ$  (Figure 3(d)), with both exhibiting equivalent values of  $\theta_{\text{obs}}$ . In addition, when  $\phi = 0^\circ$ , the

measured values of  $\theta_{\text{obs}}$  was equivalent to the intensity-weighted average polarization orientation,  $0.5 \cdot \theta_1$ . In contrast, the sum of the output of two coherent, linearly-polarized, same-wavelength sources that are not completely in-phase ( $\phi \neq 0^\circ$ ) can be differentiated from the output of a single coherent, linearly-polarized source with equivalent net intensity and the same polarization orientation as the weighted average polarization orientation of the tandem sources. In this case, the summing of the output of the tandem sources generates elliptically rather than linearly polarized illumination. The difference in the morphologies predicted by the simulations for growths with  $\phi = 0^\circ$  and  $\phi = 90^\circ$  suggests that the photoelectrodeposition process is capable of differentiating elliptically polarized from linearly polarized illumination. Hence, the resulting photoelectrodeposit physically encodes information concerning the relative phase of the illumination inputs.



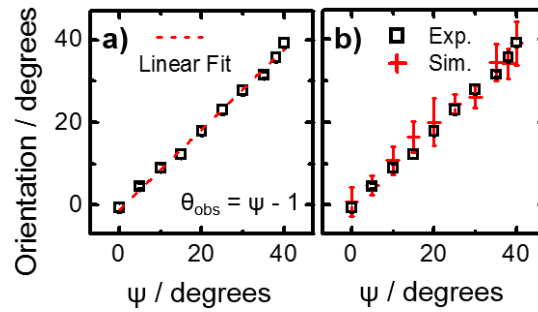
**Figure 5.4.** Effect of elliptical illumination polarization on photoelectrodeposit morphology. (a)-(d) Plots of the E-field vector traced over time at a fixed point for illumination provided by a HeNe laser  $\lambda_{\text{avg}} = 632.8 \text{ nm}$  with defined elliptical polarizations.  $\psi$  indicates the orientation of the major axis of the ellipse measured clockwise from the vertical.  $\chi$  represents the angle between the major axis and a line connecting a vertex on the major axis with one on the minor axis and relates the eccentricity and asymmetry of the ellipse. (e)-(h) SEMs representative of photoelectrodeposits generated with the elliptical illumination profiles indicated in (a)-(d), respectively.

Figure 5.4(a)-(d) presents plots of the polarization ellipses that result from the out-of-phase addition ( $\phi = 90^\circ$ ) of sources with E-field vectors the same as those

plotted in Figure 5.2(a)-(d) and thus describe the illumination utilized in the simulations presented in Figure 5.3(e)-(h). The orientation of the major axis of the ellipse, measured clockwise from the vertical, is denoted as  $\psi$ . The angle between the major axis of the ellipse and a line connecting a vertex on the major axis with one on the minor axis, denoted as  $\chi$ , quantifies the asymmetry, or eccentricity, of the ellipse. For the conditions investigated in the simulations presented in Figure 5.3(e)-(h),  $\psi = \chi = 0.5 \cdot \theta_1$ . Using these same elliptical polarizations, deposits were generated experimentally (with HeNe laser illumination with  $\lambda_{\text{avg}} = 632.8 \text{ nm}$ ) to corroborate the conclusions from the simulations that the photoelectrochemical growth process can discriminate between linearly and elliptically polarized illumination, and thus responds to phase data contained in the incident illumination. The growth modeling indicated that this phenomenon manifests itself in the degree of nanoscale pattern anisotropy, and is potentially an effect of variable anisotropy in the illumination polarization. The addition of out-of-phase orthogonal polarization components results in the generation of an elliptical polarization state, and increasing amounts of such components decreases the asymmetry of the relevant polarization ellipse (quantified by  $\chi$ ). The simulations predict that as this asymmetry is reduced beyond a threshold ( $\chi > 30^\circ$ ), the observable morphological patterning begins to transition from anisotropic to isotropic, and, in the limiting case of circular polarization ( $\chi = 45^\circ$ ), the patterning becomes completely isotropic.

Figure 5.4(e)-(h) presents SEMs of the deposits that were generated utilizing the elliptical polarizations corresponding to those presented in Figure 5.4(a)-(d). Deposition with elliptical polarization with  $\chi = 30^\circ$  (Figure 4(e)) resulted in the

generation of lamellar structures with highly uniaxial anisotropy, as in the case of linear polarization (Figure 1(b);  $\chi = 0^\circ$  equivalent). For  $\chi = 35^\circ$  (Figure 4(f)), the overall morphological anisotropy was reduced compared to the case for  $\chi = 30^\circ$ , and an isotropic mesh-type pattern was observed underlying the anisotropic lamellar pattern. For  $\chi = 40^\circ$  (Figure 4(g)), this mesh-type morphology became more prominent, with a height approaching that of the anisotropic pattern. For  $\chi = 45^\circ$  (Figure 5.4(h)), no anisotropic pattern was observed; rather, the morphology was highly similar to that produced by a single unpolarized incoherent source (Figure 5.1(d)). Thus, the experimental morphologies presented in Figure 5.4(e)-(h) matched those predicted by the growth model (Figure 5.3(e)-(h)). Such collective agreement demonstrates the capacity of the deposition to produce unique morphologies in response to elliptically polarized illumination, and thus to store relative phase information. Specifically, superimposed isotropic mesh-type patterns and anisotropic lamellar-type patterns are generated wherein the weighting between the two types of patterns is correlated with the phase difference between the orthogonal polarization components of the optical field (and thus the resultant ellipticity of the output).



**Figure 5.5.** Orientation of photoelectrodeposit morphologies generated using elliptically polarized illumination derived from experimental results and computationally via growth modeling (a) Plot of the orientation of the pattern long axis ( $\theta_{\text{obs}}$ ) measured clockwise from the vertical as a function of  $\psi$  for photoelectrodeposits generated with elliptically polarized illumination. Error bars generally smaller than displayed symbols. (b) Same as (a) but with addition of values from growth modeling.

Auxiliary information regarding the polarization state of the incident illumination is also inherent in the lamellar-type pattern, because the pattern anisotropy is associated with an orientation. To characterize the relation between an elliptical polarization and the encoded orientation, additional deposits were generated experimentally using polarizations having  $0^\circ \leq \psi \leq 25^\circ$  and  $\chi = \psi$ . Figure 5.5(a) presents values of  $\theta_{\text{obs}}$  for  $0^\circ \leq \psi \leq 40^\circ$  (wherein  $\chi = \psi$ ) as a function of  $\psi$ . The trend is well-fit by a line of the form  $\theta_{\text{obs}} = \psi - 1$ . Additional growth modeling was performed to generate simulated morphologies for all of the experimentally investigated elliptical polarizations. Figure 5.5(b) plots the values of  $\theta_{\text{obs}}$  derived from these simulations as a function of  $\psi$ , along with the corresponding experimental observations. Quantitative agreement was observed between the simulation and experiment. The near equivalence between  $\theta_{\text{obs}}$  and  $\psi$  indicates that the directional component of the anisotropy of an elliptical polarization state is directly recorded in the deposit morphology. Moreover,

this anisotropy is discernible not only when the polarization is defined by a highly asymmetric ellipse (small values of  $\chi$ , approximating linear polarization) but also when the polarization is defined by a near-circular ellipse, e.g.  $\chi = 40^\circ$  (Figure 5.4(h)). This behavior indicates that when the illumination used in the deposition process is supplied by tandem sources, the lamellar component of the morphology arises from the in-phase addition of orthogonal polarization components, whereas the mesh component arises from out-of-phase addition. This behavior and rationale is consistent with the observations of the morphologies generated using two near-orthogonal or orthogonal equal intensity incoherent sources (Figure 5.2). As observed for the analogous simulations (Figure 5.3(e)-(h)) and experiments (Figure 5.4(e)-(h)) with coherent sources with  $\phi = 90^\circ$ , only a lamellar-type morphology was observed for  $\theta_1 = 60^\circ$  ( $\theta_0 = 0^\circ$ ) whereas a lamellar-type morphology superimposed on a mesh-type was observed for  $\theta_1 = 70^\circ$  and  $80^\circ$ . In each case, the lamellar morphology was oriented along the intensity-weighted average polarization orientation. However, in contrast to deposits generated using coherent sources with  $\phi = 90^\circ$ , the lamellar morphologies were more prominent for  $\theta_1 = 70^\circ$  and  $80^\circ$ , and for  $\theta_1 = 90^\circ$ , some anisotropy was still observed. This behavior results from the presence of in-phase addition in complement to the out-of-phase addition solely present in the coherent case with  $\phi = 90^\circ$ , as the summing of the incoherent sources involves many additions with a continuous range of phase angles ( $0^\circ \leq \phi \leq 90^\circ$ ), in contrast to the coherent case for which  $\phi$  was fixed at  $90^\circ$ . Similarly, the absence of a discernible mesh-type morphological component in the incoherent case with  $\theta_1 = 60^\circ$  is consistent with an insufficient amount of out-of-phase addition of orthogonal polarization components.

### 5.3 Conclusions

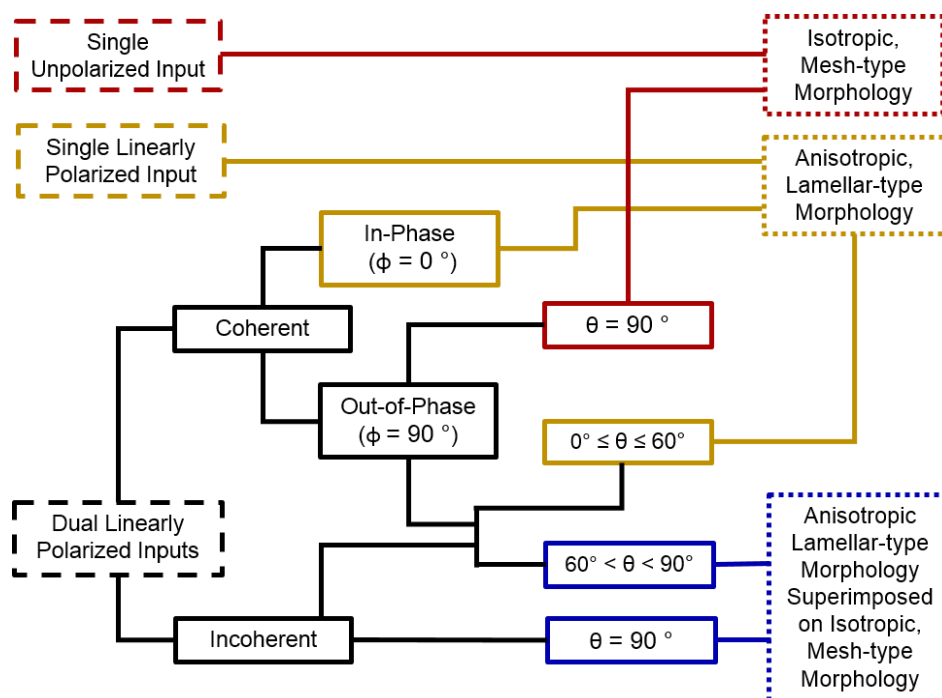


**Figure 5.6.** Flowchart detailing expected photoelectrodeposit morphology as a function of the polarization characteristics of the optical inputs.  $\theta$  represents the angle between the polarization vectors of two linearly polarized inputs and  $\phi$  represents the phase angle between two coherent inputs. Simultaneous inputs are assumed to be of equal intensity. Anisotropic morphologies orient with long axes parallel to the average polarization vector of the input(s).

Figure 5.6 presents a flowchart that outlines the morphology of the photoelectrodeposit as a function of the polarization characteristics of the optical inputs. In summary, photoelectrodeposition using a single, linearly polarized source resulted in the generation of a highly anisotropic, lamellar-type morphology, whereas the use of an unpolarized source resulted in the generation of an isotropic, mesh-type morphology. The use of tandem simultaneous same-wavelength, linearly polarized,

coherent and in-phase sources also resulted in the generation of lamellar-type structures, because such illumination is equivalent to that produced by a single linearly-polarized coherent source. Summing two linearly polarized, coherent sources that are not completely in-phase results in elliptically polarized illumination. The use of such illumination generated a spectrum of related morphologies that were dependent on the ellipticity, which correlates with the amount of out-of-phase addition between orthogonally polarized components of the optical inputs. For sufficiently low degrees of ellipticity ( $\chi \leq 30^\circ$ ), lamellar morphologies that appear equivalent to those generated using a single linearly polarized source were observed. For greater degrees of ellipticity, lamellar-type patterns were superimposed on a mesh-type pattern that was similar to the pattern observed when unpolarized illumination was used. Relative to the lamellar-type pattern, the mesh-type pattern increased in height and definition as the degree of the polarization ellipticity increased. Only the mesh-type pattern was observed in the limiting case of circular polarization ( $\chi = 45^\circ$ ). The results of deposition using two linearly polarized, incoherent sources were consistent with those observed for the use of two coherent sources that were not completely in-phase, in that anisotropic, lamellar-type morphologies transitioned to isotropic, mesh-type morphologies as the amount of out-of-phase addition increased between the orthogonally polarized components of the light sources. When tandem sources were used and lamellar-type morphologies were generated, the long axis of the lamellar pattern always aligned parallel to the intensity-weighted average polarization orientation. The observed morphologies consistently matched those simulated by computational modeling, indicating that the specific morphology was fully determined by each set of defined

optical inputs. Thus, the collective experimental and computational modeling data indicate that the photoelectrochemical growth process is sensitive to the coherency, relative phase, and polarization orientations of the utilized illumination inputs, and that the resulting morphology expresses these inputs in a distinctive pattern in each case.

## BIBLIOGRAPHY

- [1] Salem, L. Theory of Photochemical Reactions. *Science* **1976**, *191*, 822-830.
- [2] Chen, G.; Imanishi, Y.; Ito, Y. pH-Sensitive Thin Hydrogel Microfabricated by Photolithography. *Langmuir* **1998**, *14*, 6610-6612.
- [3] Revzin, A.; Russell, R. J.; Yadavalli, V. K.; Koh, W.-G.; Deister, C.; Hile, D. D.; Mellott, M. B.; Pishko, M. V. Fabrication of Poly(ethylene glycol) Hydrogel Microstructures Using Photolithography. *Langmuir* **2001**, *17*, 5440-5447.
- [4] Totzeck, M.; Ulrich, W.; Göhnermeier, A.; Kaiser, W. Pushing Deep Ultraviolet Lithography to its Limits. *Nat. Photonics* **2007**, *1*, 629-631.
- [5] Wallraff, G. M.; Hinsberg, W. D. Lithographic Imaging Techniques for the Formation of Nanoscopic Features. *Chem. Rev.* **1999**, *99*, 1801-1821.
- [6] Arnold, C. B.; Serra, P.; Piqué, A. Laser direct-write techniques for printing of complex materials. *MRS Bull.* **2007**, *32*, 23-31.
- [7] Deutsch, T. F.; Ehrlich, D. J.; Osgood, R. M. Laser photodeposition of metal films with microscopic features. *Appl. Phys. Lett.* **1979**, *35*, 175-177.
- [8] Tsao, J. Y.; Ehrlich, D. J. Patterned Photonucleation of Chemical Vapor-Deposition of Al by UV-Laser Photodeposition. *Appl. Phys. Lett.* **1984**, *45*, 617-619.
- [9] Rauh, R. D.; LeLievre, R. A. Microphotoelectrochemical Etching of n-GaAs Using a Scanned Focused Laser. *J. Electrochem. Soc.* **1985**, *132*, 2811-2812.
- [10] Attard, A. E.; Brown, D. E. Photoelectroplating Light Modulator. *Appl. Opt.* **1968**, *7*, 511-516.
- [11] Inoue, T.; Fujishima, A.; Honda, K. Photoelectrochromic Characteristics of Photoelectrochemical Imaging System with a Semiconductor/Solution (Metallic Ion) Junction. *J. Electrochem. Soc.* **1980**, *127*, 1582-1588.

- [12] Morishita, S. Photoelectrochemical Deposition of Copper on TiO<sub>2</sub> Particles. Generation of Copper Patterns without Photoresists. *Chem. Lett.* **1992**, *21*, 1979-1982.
- [13] Yoshihara, S.; Shinozaki, K.; Shirakashi, T.; Hashimoto, K.; Tryk, D. A.; Fujishima, A. Photoelectrodeposition of copper on boron-doped diamond films: application to conductive pattern formation on diamond. The photographic diamond surface phenomenon. *Electrochim. Acta* **1999**, *44*, 2711-2719.
- [14] Micheels, R. H.; Darrow, A. D.; Rauh, R. D. Photoelectrochemical deposition of microscopic metal film patterns on Si and GaAs. *Appl. Phys. Lett.* **1981**, *39*, 418-420.
- [15] Langille, M. R.; Personick, M. L.; Mirkin, C. A. Plasmon-Mediated Syntheses of Metallic Nanostructures. *Angew. Chem. Int. Ed.* **2013**, *52*, 13910-13940.
- [16] Grzelczak, M.; Liz-Marzán, L. M. The relevance of light in the formation of colloidal metal nanoparticles. *Chem. Soc. Rev.* **2014**, *43*, 2089-2097.
- [17] Gibbons, W. M.; Shannon, P. J.; Sun, S.-T.; Swetlin, B. J. Surface-Mediated Alignment of Nematic Crystals with Polarized Laser Light. *Nature* **1991**, *351*, 49-50.
- [18] Shannon, P. J.; Gibbons, W. M.; Sun, S.-T. Patterned Optical Properties in Photopolymerized Surface-Aligned Liquid-Crystal Films. *Nature* **1994**, *368*, 532-533.
- [19] Ichimura, K. Photoalignment of Liquid-Crystal Systems. *Chem. Rev.* **2000**, *100*, 1847-1873.
- [20] Barrett, C. J.; Nathansohn, A. L.; Rochon, P. L. Mechanism of Optically Inscribed High-Efficiency Diffraction Gratings in Azo Polymer Films. *J. Phys. Chem.* **1996**, *100*, 8836-8842.
- [21] Dasog, M.; Carim, A. I.; Yalamanchili, S.; Atwater, H. A.; Lewis, N. S. Profiling Photoinduced Carrier Generation in Semiconductor Microwire

- Arrays via Photoelectrochemical Metal Deposition. *Nano Lett.* **2016**, *16*, 5015-5021.
- [22] Kontoleta, E.; Askes, S. H. C.; Lai, L. H.; Garnett, E. C. Localized photodeposition of catalysts using nanophotonic resonances in silicon photocathodes. *Beilstein J. Nanotechnol.* **2018**, *9*, 2097-2105.
- [23] Hubert, C.; Rumyantseva, A.; Lerondel, G.; Grand, J.; Kostcheev, S.; Billot, L.; Vial, A.; Bachelot, R.; Royer, P.; Chang, S.-h.; Gray, S. K.; Wiederrecht, G. P.; Schatz, G. C. Near-Field Photochemical Imaging of Noble Metal Nanostructures. *Nano Lett.* **2005**, *5*, 615-619.
- [24] Hubert, C.; Bachelot, R.; Plain, J.; Kostcheev, S.; Lerondel, G.; Juan, M.; Royer, P.; Zou, S.; Schatz, G. C.; Wiederrecht, G. P.; Gray, S. K. Near-Field Polarization Effects in Molecular-Motion-Induced Photochemical Imaging. *J. Phys. Chem. C* **2008**, *112*, 4111-4116.
- [25] Plain, J.; Wiederrecht, G. P.; Gray, S. K.; Royer, P.; Bachelot, R. Multiscale Optical Imaging of Complex Fields Based on the Use of Azobenzene Nanomotors. *J. Phys. Chem. Lett.* **2013**, *4*, 2124-2132.
- [26] Ishitobi, H.; Nakamura, I.; Kobayashi, T.-a.; Hayazawa, N.; Sekkat, Z.; Kawata, S.; Inouye, Y. Nanomovement of Azo Polymers Induced by Longitudinal Fields. *ACS Photonics* **2014**, *1*, 190-197.
- [27] Jin, R.; Cao, Y. C.; Hao, E.; Métraux, G. S.; Schatz, G. C.; Mirkin, C. A. Controlling anisotropic nanoparticle growth through plasmonic excitation. *Nature* **2003**, *425*, 487-490.
- [28] Maillard, M.; Huang, P.; Brus, L. Silver Nanodisk Growth by Surface Plasmon Enhanced Photoreduction of Adsorbed  $[Ag^+]$ . *Nano Lett.* **2003**, *3*, 1611-1615.
- [29] Paul, A.; Kenens, B.; Hofkens, J.; Uji-i, H. Excitation Polarization Sensitivity of Plasmon-Mediated Silver Nanotriangle Growth on a Surface. *Langmuir* **2012**, *28*, 8920-8925.

- [30] Shell, G. S. G.; Lang, A. R. G. Description of Leaf Orientation and Heliotropic Response of Sunflower Using Directional Statistics. *Agric. Meteorol.* **1975**, *15*, 33-48.
- [31] Ehleringer, J.; Forseth, I. Solar Tracking by Plants. *Science* **1980**, *210*, 1094-1098.
- [32] Thanisawanyangkura, S.; Sinoquet, H.; Rivet, P.; Cretenet, M.; Jallas, E. Leaf Orientation and sunlit leaf area distribution in cotton. *Agric. For. Meteorol.* **1997**, *86*, 1-15.
- [33] Shell, G. S. G.; Lang, A. R. G.; Sale, P. J. M. Quantitative Measures of Leaf Orientation and Heliotropic Response in Sunflower, Bean, Pepper, and Cucumber. *Agric. Meteorol.* **1974**, *13*, 25-37.
- [34] Garrey, W. E. Light and the Muscle Tonus of Insects. The Heliotropic Mechanism. *J. Gen. Physiol.* **1918**, *1*, 101-125.
- [35] Loeb, J.; Northrop, J. H. Heliotropic Animals as Photometers on the basis of the validity of the Bunsen-Roscoe Law for Heliotropic Reactions. *Proc. Natl. Acad. Sci. U. S. A.* **1917**, *3*, 539-544.
- [36] Li, C.; Liu, Y.; Huang, X.; Jiang, H. Direct Sun-Driven Artificial Heliotropism for Solar Energy Harvesting Based on a Photo-Thermomechanical Liquid-Crystal Elastomer Nanocomposite. *Adv. Funct. Mater.* **2012**, *22*, 5166-5174.
- [37] Deng, J.; Li, J.; Chen, P.; Fang, X.; Sun, X.; Jiang, Y.; Weng, W.; Wang, B.; Peng, H. Tunable Photothermal Actuators Based on a Pre-programmed Aligned Nanostructure. *J. Am. Chem. Soc.* **2016**, *138*, 225-230.
- [38] Vassalini, I.; Alessandri, I. "The phactalysts": carbon nanotube/TiO<sub>2</sub> composites as phototropic actuators for wireless remote triggering of chemical reactions and catalysis. *Nanoscale* **2017**, *9*, 11446-11451.
- [39] Palagi, S.; Mark, A. G.; Reigh, S. Y.; Melde, K.; Qiu, T.; Zeng, H.; Parmeggiani, C.; Martella, D.; Sanchez-Castillo, A.; Kapernaum, N.; Giesselmann, F.; Wiersma, D. S.; Lauga, E.; Fischer, P. Structured light

- enables biomimetic swimming and versatile locomotion of photoresponsive soft microrobots. *Nat. Mater.* **2016**, *15*, 647-653.
- [40] Tomlinson, P. B. *The Structural Biology of Palms*; Oxford University Press: New York, 1990.
- [41] Christie, J. M.; Murphy, A. S. Shoot phototropism in higher plants: New light through old concepts. *Am. J. Bot.* **2013**, *100*, 35-46.
- [42] Iwase, A.; Sakai, K.; Suzuki, A.; van Woesik, R. Phototropic adjustment of the foliaceous coral *Echinopora lamellosa* in Palau. *Estuar. Coast. Shelf Sci.* **2008**, *77*, 672-678.
- [43] Kaniewska, P.; Campbell, P. R.; Fine, M.; Hoegh-Guldberg, O. Phototropic growth in a reef flat acroporid branching coral species. *J. Exp. Biol.* **2009**, *212*, 662-667.
- [44] Hutchings, M. J.; de Kroon, H. Foraging in Plants: the Role of Morphological Plasticity in Resource Acquisition. In *Advances in Ecological Research*; Begon, M., Fitter, A. H., Eds.; Academic Press: London, 1994; Vol. 25, pp 159-238.
- [45] Slade, A. J.; Hutchings, M. J. The Effects of Light Intensity on Foraging in the Clonal Herb *Glechoma Hederacea*. *J. Ecol.* **1987**, *75*, 639-650.
- [46] Meier, M. C.; Cheng, W.-H.; Atwater, H. A.; Lewis, N. S.; Carim, A. I. Inorganic Phototropism in Electrodeposition of Se-Te. *J. Am. Chem. Soc.* **2019**, *141*, 18658-18661.
- [47] Sadtler, B.; Burgos, S. P.; Batara, N. A.; Beardslee, J. A.; Atwater, H. A.; Lewis, N. S. Phototropic growth control of nanoscale pattern formation in photoelectrodeposited Se-Te films. *Proc. Natl. Acad. Sci. U. S. A.* **2013**, *110*, 19707-19712.
- [48] Tan, C.; Qin, C.; Sadtler, B. Light-directed growth of metal and semiconductor nanostructures. *J. Mater. Chem. C* **2017**, *5*, 5628-5642.
- [49] Yin, A. J.; Li, J.; Jian, W.; Bennett, A. J.; Xu, J. M. Fabrication of Highly Ordered Metallic Nanowire Arrays by Electrodeposition. *Appl. Phys. Lett.* **2001**, *79*, 1039.

- [50] Sander, M. S.; Prieto, A. L.; Gronsky, R.; Stacy, A. M. Fabrication of High-Density, High Aspect Ratio, Large-Area Bismuth Telluride Nanowire Arrays by Electrodeposition into Porous Anodic Alumina Templates. *Adv. Mater.* **2002**, *14*, 665-667.
- [51] Choi, K.-S.; Lichtenegger, H. C.; Stucky, G. D.; McFarland, E. W. Electrochemical Synthesis of Nanostructured ZnO Films Utilizing Self-Assembly of Surfactant Molecules at Solid-Liquid Interfaces. *J. Am. Chem. Soc.* **2002**, *124*, 12402-12403.
- [52] Choi, K.-S. Shape Control of Inorganic Materials via Electrodeposition. *Dalton Trans.* **2008**, 5432-5438.
- [53] Xiao, Z.-L.; Han, C. Y.; Kwok, W.-K.; Wang, H.-H.; Welp, U.; Wang, J.; Crabtree, G. W. Tuning the Architecture of Mesosstructures by Electrodeposition. *J. Am. Chem. Soc.* **2004**, *126*, 2316-2317.
- [54] Siegfried, M. J.; Choi, K.-S. Elucidating the Effect of Additives on the Growth and Stability of Cu<sub>2</sub>O Surfaces via Shape Transformation of Pre-Grown Crystals. *J. Am. Chem. Soc.* **2006**, *128*, 10356-10357.
- [55] Liu, R.; Vertegel, A. A.; Bohannon, E. W.; Sorenson, T. A.; Switzer, J. A. Epitaxial Electrodeposition of Zinc Oxide Nanopillars on Single-Crystal Gold. *Chem. Mater.* **2001**, *13*, 508-512.
- [56] Carim, A. I.; Hamann, K. R.; Batara, N. A.; Thompson, J. R.; Atwater, H. A.; Lewis, N. S. Template-Free Synthesis of Periodic Three-Dimensional PbSe Nanostructures via Photoelectrodeposition. *J. Am. Chem. Soc.* **2018**, *140*, 6536-6539.
- [57] Hamann, K. R.; Carim, A. I.; Meier, M. C.; Thompson, J. R.; Batara, N. A.; Yermolenko, I. S.; Atwater, H. A.; Lewis, N. S. Optically tunable mesoscale CdSe morphologies via inorganic phototropic growth. *J. Mater. Chem. C* **2020**, 12412-12417.
- [58] Carim, A. I.; Batara, N. A.; Premkumar, A.; Atwater, H. A.; Lewis, N. S. Self-Optimizing Photoelectrochemical Growth of Nanopatterned Se-Te

Films in Response to the Spectral Distribution of Incident Illumination.

*Nano Lett.* **2015**, *15*, 7071-7076.

- [59] Carim, A. I.; Batara, N. A.; Premkumar, A.; Atwater, H. A.; Lewis, N. S. Polarization Control of Morphological Pattern Orientation During Light-Mediated Synthesis of Nanostructured Se-Te Films. *ACS Nano* **2016**, *10*, 102-111.
- [60] Carim, A. I.; Batara, N. A.; Premkumar, A.; May, R.; Atwater, H. A.; Lewis, N. S. Morphological Expression of the Coherence and Relative Phase of Optical Inputs to the Photoelectrodeposition of Nanopatterned Se-Te Films. *Nano Lett.* **2016**, *16*, 2963-2968.
- [61] Hamann, K. R.; Carim, A. I.; Meier, M. C.; Lewis, N. S. Path-Dependent Morphological Evolution of Se-Te Mesostructures Prepared by Inorganic Phototropic Growth. *J. Am. Chem. Soc.* **2020**, *142*, 19840-19843.
- [62] Carim, A. I.; Meier, M. C.; Kennedy, K. M.; Richter, M. H.; Hamann, K. R.; Lewis, N. S. Assessing Effects of Near-Field Synergistic Light Absorption on Ordered Inorganic Phototropic Growth. *J. Am. Chem. Soc.* **2021**, *143*, 3693-3696.
- [63] Hale, G. M.; Querry, M. R. Optical Constants of Water in the 200-nm to 200- $\mu$ m Wavelength Region. *Appl. Opt.* **1973**, *12*, 555-563.
- [64] Brueck, S. R. J.; Ehrlich, D. J. Stimulated Surface-Plasma-Wave Scattering and Growth of a Periodic Structure in Laser-Photodeposited Metal Films. *Phys. Rev. Lett.* **1982**, *48*, 1678-1681.
- [65] Osgood, R. M.; Ehrlich, D. J. Optically induced microstructures in laser-photodeposited metal films. *Opt. Lett.* **1982**, *7*, 385-387.
- [66] Destouches, N.; Crespo-Monteiro, N.; Vitrant, G.; Lefkir, Y.; Reynaud, S.; Epicier, T.; Liu, Y.; Vocanson, F.; Pigeon, F. Self-organized growth of metallic nanoparticles in a thin film under homogeneous and continuous-wave light excitation. *J. Mater. Chem. C* **2014**, *2*, 6256-6263.
- [67] Sipe, J. E.; Young, J. F.; Preston, J. S.; van Driel, H. M. Laser-induced periodic surface structure. I. Theory. *Phys. Rev. B* **1983**, *27*, 1141-1154.

- [68] Young, J. F.; Preston, J. S.; van Driel, H. M.; Sipe, J. E. Laser-induced periodic surface structure. II. Experiments on Ge, Si, Al, and brass. *Phys. Rev. B* **1983**, *27*, 1155-1172.
- [69] Kildishev, A. V.; Boltasseva, A.; Shalaev, V. M. Planar Photonics with Metasurfaces. *Science* **2013**, *339*, 1232009.
- [70] Verslegers, L.; Catrysse, P. B.; Yu, Z.; White, J. S.; Barnard, E. S.; Brongersma, M. L.; Fan, S. Planar Lenses Based on Nanoscale Slit Arrays in a Metallic Film. *Nano Lett.* **2009**, *9*, 235-238.
- [71] Fattal, D.; Li, J.; Peng, Z.; Fiorentino, M.; Beausoleil, R. G. Flat Dielectric Grating Reflectors with Focusing Abilities. *Nat. Photonics* **2009**, *4*, 466-470.
- [72] Gansel, J. K.; Thiel, M.; Rill, M. S.; Decker, M.; Bade, K.; Saile, V.; von Freymann, G.; Linden, S.; Wegener, M. Gold Helix Photonic Metamaterial as Broadband Circular Polarizer. *Science* **2009**, *325*, 1513-1515.
- [73] Chen, Z.; Cummins, D.; Reinecke, B. N.; Clark, E.; Sunkara, M. K.; Jaramillo, T. F. Core-shell MoO<sub>3</sub>-MoS<sub>2</sub> Nanowires for Hydrogen Evolution: A Functional Design for Electrocatalytic Materials. *Nano Lett.* **2011**, *11*, 4168-4175.
- [74] Kong, D.; Wang, H.; Lu, Z.; Cui, Y. CoSe<sub>2</sub> Nanoparticles Grown on Carbon Fiber Paper: An Efficient and Stable Electrocatalyst for Hydrogen Evolution Reaction. *J. Am. Chem. Soc.* **2014**, *136*, 4897-4900.